Numerical study of expansion tube problems: Toward the simulation of cavitation

Eric Goncalvès da Silva

HAL Id: hal-00767725
https://hal.science/hal-00767725

Submitted on 2 Jan 2013

Numerical study of expansion tube problems: toward the simulation of cavitation

Eric Goncalvès[*]

LEGI-University of Grenoble, 1025 rue de la Piscine, 38400 St Martin d'Heres, France

Abstract

A compressible, multiphase, one-fluid inviscid solver has been developed to investigate the behaviour of various cavitation models. A new source term for the mass transfer between phases is proposed. A range of models from three to five equations is compared. Numerical simulations are performed on rarefaction problems and compared with reference solutions.

Keywords: Two-phase flow, Cavitation, Homogeneous model, Mass transfer, Euler simulation

1. Introduction

Cavitation is a significant engineering phenomenon that occurs in fluid machinery, fuel injectors, marine propellers, nozzles, underwater bodies, etc. In most cases, cavitation is an undesirable phenomenon, significantly degrading performance, resulting in reduced flow rates, lower pressure increases in pumps, load asymmetry, vibrations, noise and erosion. Such flows are characterized by important variations of the local Mach number (due to the drastic

---

[*]Corresponding author.
  Email address: `Eric.Goncalves@legi.grenoble-inp.fr` (Eric Goncalvès)

diminution of the speed of sound in the mixture), large density ratio between the liquid and the vapor phases, compressibility effects on turbulence and thermodynamic phase transition.

Several physical and numerical models have been developed to investigate cavitating flows within the class of averaged two-phase flow models. This method makes no attempt to track the liquid and vapour interface. As most two-phase flows have extremely complicated interfacial geometry and motions, it is not possible to solve for local instant motions of the fluid particles. By proper averaging, the mean values of fluid motions and properties can be obtained. In its implementation, there are different approaches according to the assumptions made on the local thermodynamic equilibrium and the slip condition between phases. A hierarchy of models exists, with the numbers of equations ranging from seven to three only. The full non-equilibrium seven-equation models are the most complete. For both fluids, it contains equations for the mass, momentum and energy, and the seventh equation describes the topology of the flow. Because the exchanges of mass, momentum and energy are treated explicitly as transfer terms, these models can take into account the physical details occurring in the cavitation phenomenon such as mass exchange, thermal transfer and surface tension. However, the transfer terms have to be known; such quantities are usually very difficult to obtain. Various formulations have been investigated to deal with metastable states and evaporation front dynamics, derived from the seven-equation model of Baer-Nunziato [1]. Such models have been used for inviscid high-speed cavitating applications and two-phase Riemann problems [2, 3, 4, 5]. For thermal-

2

hydraulics applications with cavitation, nucleation and boiling flows, a six-equation model has been developed [6, 7]. The interfacial mass transfer is modeled as a function of the interfacial heat transfer terms and the interfacial phase-averaged enthalpies. Since the general physics is not always necessary, simpler and more compact models have been proposed and successfully applied for cavitating flows.

An important class of reduced models is formed by the five-equation models, in which velocity equilibrium and pressure equilibrium are considered. The archetype five-equation model is that of Kapila [8]. It is composed of four conservation laws: two for masses, one for the mixture momentum and one for the mixture energy. It is completed by an equation for a non-conservative quantity describing the flow topology, usually the void ratio. Such a model has been used for inviscid high speed cavitating applications and cavitation pocket in fuel injector nozzles [9, 10, 11]. Other formulations have been proposed [12, 13, 14] but have not found application in cavitation. For a clear and compact overview over existing reduced two-fluid flow models, we refer to [15].

By assuming the thermal equilibrium between phases, a four-equation model can be expressed. A very popular formulation has been developed to simulate turbulent cavitating flows [16, 17, 18, 19, 20, 21, 22, 23, 24, 25]. It is composed by three conservation laws for mixture quantities (mass, momentum, energy) plus a mass equation for the vapour or liquid density including a cavitation source term. The main difficulty is related to the formulation of the source term and the tunable parameters involved for the vaporization and condensation processes (different sets of parameters are presented

in [23]). Another popular model devoted to ebullition problems uses a mass fraction equation with a relaxation term (homogeneous relaxation model). The source term involves a relaxation time that is the time for the system to regain its thermodynamic equilibrium state. This time is very difficult to determine and is estimated from experimental data [26, 27, 28]. An original approach of the relaxation term was proposed in [29], based on a constrained convex optimization problem on the mixture entropy.

With the assumption of complete thermodynamic equilibrium between phases (local temperature, pressure and free Gibbs enthalpy equality between phases), we obtain the 3-equation models or homogeneous equilibrium models (HEM). Vaporization or condensation processes are assumed to be instantaneous. An equation of state (EOS) is necessary to close the system. Different closure relations (tabulated EOS or combination of pure phase EOSs) that link the pressure to the thermodynamic variables have been proposed [30, 31, 32, 33, 34, 35, 36, 37, 38, 39, 40, 41, 42, 43, 44, 45]. Other EOS have been investigated using an entropy maximization procedure [46, 47]. Small non-equilibrium effects can be introduced in the EOS compared to an isothermal thermodynamic path. When non-equilibrium effect becomes important, additional equations are needed for an accurate prediction.

A critical aspect for cavitating simulations concerns the numerical methods and accuracy problems. Characteristics of cavitating flows make the simulation very stiff and challenging. Among them, large variations of the speed of sound in the mixture is a difficult problem. Indeed, the speed of sound can be several orders of magnitude higher in the liquid phase than in the

4

two-phase mixture. The non-monotonic behavior of the sound speed in the mixture causes inaccuracies in wave's transmission across interfaces. Moreover, volume fraction variation across acoustic waves results in difficulties for the Riemann problem resolution, and in particular for the derivation of approximate solvers [11]. Volume fraction positivity in the presence of shocks or strong expansion waves is another issue resulting in lack of robustness. The presence of large discontinuities of thermodynamic variables and equations of state at material interfaces result in numerical instabilities and spurious oscillations [48]. The reason lies in the numerical dissipation of the schemes which mimic a thermodynamic path that is not correct. Finally, the large decrease of the pressure up to vacuum apparition leads to computational failure for Godunov methods. To circumvent these difficulties, equilibrium assumptions are relaxed, especially the pressure equilibrium condition, which results in the non-conservative equation for the volume fraction [11, 49].

On the other hand, for turbulent cavitating applications computed with three- or four-equation models, various shock-capturing schemes developed for aerodynamic problems have been extended to cavitating flows: AUSM family [34, 50, 42], Jameson [51, 43, 44], Roe [22, 41, 52, 53], Rusanov [54] and flux difference splitting procedure [17].

In fact, the more sophisticated models with relaxation procedures have been tested on inviscid high-speed applications, whereas the simplest models associated with shock-capturing schemes have been massively used for industrial cavitating flows. The present work is part of a research aimed at developing a numerical tool devoted to turbulent cavitating flows for which both the

computation cost and the quality of results are acceptable. The simplicity of the model and the numerical integration is privileged. In previous works, the dependence of solutions on the turbulence modelling and the wall model (in the framework of RANS compressible 1-fluid equations) has been illustrated in computing cavitation pockets on Venturi geometries [55, 56]. The interplay between turbulence and cavitation regarding the unsteadiness and structure of the flow is complex and not well understood. As a consequence, only inviscid simulations are proposed in the present study to isolate the cavitation model effect and to evaluate its capacity to reproduce a phase transition with non equilibrium effects.

A new source term for the mass transfer between phases is proposed and introduced on both a four-equation and a five-equation model. We compared these new models with two popular models largely used in cavitation simulations: the sinusoidal barotropic three-equation model and the Hosangadi four-equation model. Our goals in respect to the cavitation modelling are:

- To validate the new source term formulation.

- To compare the new model with other popular cavitation models. A focus on the mixture speed of sound is proposed.

- To investigate the influence of constants of models, especially for the Hosangadi model which involves two empirical parameters.

Moreover, with respect to the numerical flux computation, various schemes are tested (Jameson, Rusanov, AUSM-type, VF Roe and HLLC) to evaluate their capability to integrate this very stiff system. Different test cases are

considered: rarefaction problems with a large depression leading to evaporation, and a shock-cavitation interaction with condensation. Numerical results are validated with reference solutions computed with two-fluid solvers.

This paper is organized as follows. We first review the theoretical formulation without phase transition. We introduce the mass transfer between phases. Various test cases are presented with comparisons between models and validations against 7-equation solutions. Finally, conclusions and future investigations are discussed.

2. Formulation without phase transition

The homogeneous mixture approach is used to model two-phase flows. The phases are assumed to be sufficiently well mixed and the disperse particle size are sufficiently small thereby eliminating any significant relative motion. The phases are strongly coupled and moving at the same velocity. In addition, the phases are assumed to be in thermal and mechanical equilibrium: they share the same temperature T and the same pressure P. The evolution of the two-phase flow can be described by the conservation laws that employ the representative flow properties as unknowns just as in a single-phase problem. We introduce α_k the void fraction or the averaged fraction of presence of phase k. The density ρ, the center of mass velocity u and the internal energy e for the mixture are defined by [57]:

$$\rho = \sum_k \alpha_k \rho_k \tag{1}$$

$$\rho u = \sum_k \alpha_k \rho_k u_k \tag{2}$$

7

$$\rho e \;=\; \sum_k \alpha_k \rho_k e_k \tag{3}$$

Different two-phase models are proposed based on conservation laws written for mixture or phases quantities. To close the system, an equation of state (EOS) and a thermal relation are necessary to link the pressure and the temperature to the internal energy and the density.

2.1. The pure phases EOS

In the present study, we used the convex stiffened gas EOS for the pure phases (see [58]):

$$P(\rho, e) \;=\; (\gamma - 1)\rho(e - q) - \gamma P_\infty \tag{4}$$

$$P(\rho, T) \;=\; \rho(\gamma - 1)C_v T - P_\infty \tag{5}$$

$$T(\rho, h) \;=\; \frac{h - q}{C_p} \tag{6}$$

where $\gamma = C_p/C_v$ is the heat capacity ratio, C_p and C_v are thermal capacities, q the energy of the fluid at a given reference state and P_∞ is a constant reference pressure. The speed of sound c is given by:

$$c^2 \;=\; \gamma \frac{P + P_\infty}{\rho} \;=\; (\gamma - 1)C_p T \tag{7}$$

2.2. The mixture EOS

On the basis of the stiffened gas EOS for each pure phase, an expression for the pressure and the temperature can be deduced from the thermal and mechanical equilibrium assumption [10]. These expressions are available in all possible fluid states, function of the void ratio $\alpha = \alpha_v$ and the vapour mass fraction $Y = Y_v$:

$$P(\rho, e, \alpha, Y) \;=\; (\gamma(\alpha) - 1)\rho(e - q(Y)) - \gamma(\alpha)P_\infty(\alpha) \tag{8}$$

8

$$\frac{1}{\gamma(\alpha) - 1} = \frac{\alpha}{\gamma_v - 1} + \frac{1 - \alpha}{\gamma_l - 1} \tag{9}$$

$$q(Y) = Y q_v + (1 - Y) q_l \tag{10}$$

$$P_\infty(\alpha) = \frac{\gamma(\alpha) - 1}{\gamma(\alpha)} \left[\alpha \frac{\gamma_v}{\gamma_v - 1} P_\infty^v + (1 - \alpha) \frac{\gamma_l}{\gamma_l - 1} P_\infty^l \right] \tag{11}$$

$$T(\rho, h, Y) = \frac{h_l - q_l}{C_{p_l}} = \frac{h_v - q_v}{C_{p_v}} = \frac{h - q(Y)}{C_p(Y)} \tag{12}$$

$$C_p(Y) = Y C_{p_v} + (1 - Y) C_{p_l} \tag{13}$$

Without mass transfer, the propagation of acoustic waves follows the Wood or Wallis speed of sound [59]. This speed c_{wallis} is expressed as a weighted harmonic mean of speeds of sound of each phase:

$$\frac{1}{\rho c_{wallis}^2} = \frac{\alpha}{\rho_v c_v^2} + \frac{1 - \alpha}{\rho_l c_l^2} \tag{14}$$

2.3. A five-equation model

We consider a variant of the reduced model proposed by Kapila [8]. The model consists in mixture balance laws for momentum and energy, balance laws for mass of each pure phase and an additional equation for the void ratio. In order to simplify the formulation, we present below the inviscid one-dimensional equations, expressed in variables $w = (\alpha_l \rho_l, \alpha \rho_v, \rho u, \rho E, \alpha)$:

$$\frac{\partial \alpha_l \rho_l}{\partial t} + \frac{\partial \alpha_l \rho_l u}{\partial x} = 0 \tag{15}$$

$$\frac{\partial \alpha \rho_v}{\partial t} + \frac{\partial \alpha \rho_v u}{\partial x} = 0 \tag{16}$$

$$\frac{\partial (\rho u)}{\partial t} + \frac{\partial (\rho u^2 + P)}{\partial x} = 0 \tag{17}$$

$$\frac{\partial (\rho E)}{\partial t} + \frac{\partial (\rho u H)}{\partial x} = 0 \tag{18}$$

$$\frac{\partial \alpha}{\partial t} + u \frac{\partial \alpha}{\partial x} = \underbrace{\left(\frac{\rho_l c_l^2 - \rho_v c_v^2}{\frac{\rho_l c_l^2}{1 - \alpha} + \frac{\rho_v c_v^2}{\alpha}} \right)}_{= K} \frac{\partial u}{\partial x} \tag{19}$$

9

where $E = e + u^2/2$ denotes the mixture total energy and $H = h + u^2/2$ the mixture total enthalpy.

The five equations form a system of conservation laws having a hyperbolic nature. The eigenvalues of the system are:

$\lambda_1 = u - c_{wallis}$, $\lambda_{2,3,4} = u$ and $\lambda_5 = u + c_{wallis}$.

2.4. A four-equation model

We modify the previous model assuming the liquid is at its saturation state. The model consists in three conservation laws for mixture quantities and the additional equation for the void ratio:

$$\frac{\partial \rho}{\partial t} + \frac{\partial \rho u}{\partial x} = 0 \tag{20}$$

$$\frac{\partial (\rho u)}{\partial t} + \frac{\partial (\rho u^2 + P)}{\partial x} = 0 \tag{21}$$

$$\frac{\partial (\rho E)}{\partial t} + \frac{\partial (\rho u H)}{\partial x} = 0 \tag{22}$$

$$\frac{\partial \alpha}{\partial t} + \alpha \frac{\partial u}{\partial x} = K \frac{\partial u}{\partial x} \tag{23}$$

The pressure and temperature in the mixture follow the same relation presented above. To compute the mixture speed of sound, the system is written with the primitive variable (α, P, u, e). We introduce the quantity $C = \rho_v c_v^2 \left(1 + \frac{K}{\alpha}\right) = \rho c_{wallis}^2$.

$$\frac{\partial}{\partial t} \begin{pmatrix} \alpha \\ P \\ u \\ e \end{pmatrix} + \begin{bmatrix} u & 0 & -K & 0 \\ 0 & u & C & 0 \\ 0 & 1/\rho & u & 0 \\ 0 & 0 & P/\rho & u \end{bmatrix} \frac{\partial}{\partial x} \begin{pmatrix} \alpha \\ P \\ u \\ e \end{pmatrix} = 0$$

The eigenvalues of the matrix of the system can be easily computed. The system is hyperbolic, eigenvalues are (u-c_{wallis}, u, u, u+c_{wallis}). Eigenvectors and characteristic relations are given in Appendix A.

3. The phase transition modelling

We added the mass transfer between phases $\dot{m}$ in the formulation of the 4- and 5-equation models. The void ratio equation becomes (the demonstration for a five-equation model is given in [10]):

$$\frac{\partial \alpha}{\partial t} + u\frac{\partial \alpha}{\partial x} = K\frac{\partial u}{\partial x} + \underbrace{\left(\frac{\frac{c_v^2}{\alpha} + \frac{c_l^2}{1-\alpha}}{\frac{\rho_l c_l^2}{1-\alpha} + \frac{\rho_v c_v^2}{\alpha}}\right)}_{=1/\rho_I \text{ the interfacial density}} \dot{m} \qquad (24)$$

Different formulation for the mass transfer $\dot{m}$ are proposed in the literature. In cavitating simulations, a very popular model is based on an empirical source term splitted into two contributions for the evaporation and condensation processes. Moreover, another class of models based on three mixture conservation laws with thermodynamic equilibrium assumptions is also largely used in cavitation. The void ratio is computed with an algebraic relation without any explicit source term. To close the system, an equation of state (EOS) is necessary to link the pressure to the thermodynamic variables. In the following, we present a simple cavitation model with a barotropic sinusoidal EOS.

3.1. A barotropic model

The sinusoidal barotropic law [30, 43] is considered for the mixture. This law is characterized by its maximum slope $1/c_{baro}^2$. The quantity c_{baro} is an

11

adjustable parameter of the model, which can be interpreted as the minimum speed of sound in the mixture.

When the pressure is between $P_{vap} + \Delta P$ and $P_{vap} - \Delta P$, the following relationship applies:

$$P = P_{vap} + \left(\frac{\rho_l^{sat} - \rho_v^{sat}}{2} \right) c_{baro}^2 \operatorname{Arcsin} (1 - 2\alpha) \qquad (25)$$

where ΔP represents the pressure range of the law and, for a void ratio value of 0.5, the pressure is equal to the saturation pressure P_{vap}. This law introduces a small non-equilibrium effect on the pressure. The cavitation phenomenon is assumed to be isothermal and thermodynamic effects are neglected.

The void ratio is computed with saturation values of densities:

$$\alpha = \frac{\rho - \rho_l^{sat}}{\rho_v^{sat} - \rho_l^{sat}} \qquad (26)$$

The speed of sound in the mixture can be computed easily:

$$c^2 = \left(\frac{\partial P}{\partial \rho} \right)_s = \left(\frac{\partial P}{\partial \rho} \right)_T = \frac{c_{baro}^2}{2\sqrt{\alpha(1-\alpha)}} \qquad (27)$$

The system is hyperbolic with eigenvalues $(u - c, u, u + c)$.

Properties of the model (such as convexity conditions of the EOS) and the influence of the parameter c_{baro} have been studied in [43].

3.2. A source term based on the barotropic model

From the void ratio equation (24), a pressure equation is deduced (see Appendix B):

$$\frac{\partial P}{\partial t} + u \frac{\partial P}{\partial x} + \rho c_{wallis}^2 \frac{\partial u}{\partial x} = \frac{c_v^2}{\alpha}(1 - \frac{\rho_v}{\rho_I})\dot{m} \qquad (28)$$

12

To establish a link with the pressure equation expressed as

$$\frac{\partial P}{\partial t} + u\frac{\partial P}{\partial x} + \rho c^2 \frac{\partial u}{\partial x} = 0 \tag{29}$$

a possibility is to assume that the mass transfer is proportional to the divergence of the velocity: $\dot{m} = Z\frac{\partial u}{\partial x}$. Therefore, we have the relation:

$$\rho c^2 = \frac{\rho_l c_l^2 \rho_v c_v^2 \left[1 - Z\frac{\rho_l - \rho_v}{\rho_l \rho_v}\right]}{\alpha \rho_l c_l^2 + (1-\alpha)\rho_v c_v^2} \quad \text{or} \quad \frac{1}{\rho c^2} = \frac{1}{\rho c_{wallis}^2} \times \frac{1}{1 - Z\frac{\rho_l - \rho_v}{\rho_l \rho_v}} \tag{30}$$

To ensure a thermodynamic coherence, the mixture speed of sound has to vary between the Wallis and the equilibrium ones c_{eq}. When exchanges of mass and heat between phases are involved, the sound speed decreases to the thermodynamic equilibrium one [60]. This limit speed is evaluated with the assumption of local thermodynamic equilibrium: equalities of pressure, temperature and free enthalpy $g = h - Ts$ between phases. An expression of the speed of sound c_{eq} is given in [61].

The speed of sound of the barotropic model presented previously respects this inequality, except when the void ratio is close to 1. We propose to evaluate the quantity Z by identification with the barotropic speed of sound, we obtain

$$Z = \frac{\rho_l \rho_v}{\rho_l - \rho_v}\left[1 - \frac{c_{baro}^2}{2c_{wallis}^2}\frac{1}{\sqrt{\alpha(1-\alpha)}}\right] \tag{31}$$

Finally, the source term is

$$\dot{m} = \left[\frac{\rho_l c_l^2 - \rho_v c_v^2}{\frac{\rho_l c_l^2}{1-\alpha} + \frac{\rho_v c_v^2}{\alpha}} + \frac{\rho_l \rho_v}{\rho_I(\rho_l - \rho_v)}\left(1 - \frac{c_{baro}^2}{2c_{wallis}^2}\frac{1}{\sqrt{\alpha(1-\alpha)}}\right)\frac{\text{Min}\,(0, P - P_{vap})}{P - P_{vap}}\right]\frac{\partial u}{\partial x} \tag{32}$$

In the solver, we added a limiter on the void ratio to avoid the singular value $\alpha = 1$. This source term can also be used with the 5-equation model. In

13

the following, such models will be denoted as 4- and 5-equation barotropic models.

The thermodynamic assumptions of the proposed barotropic models are summarized in Table 1. In addition, assumptions for the 5-equation Kapila model and the 3-equation equilibrium model are presented.

3.3. An empirical source term

A class of cavitation models introduces a mass transfer between phases involving a separate contribution for vaporization and condensation processes. Two tunable parameters are associated for each process. This empirical source term can be calibrated with experimental data base. Different formulations and sets of parameters are presented in [23].

In this study, we used a formulation derived from the model proposed by Hosangadi and Ahuja [22]:

$$\dot{m} = \dot{m}^+ + \dot{m}^- = C_{prod}\frac{\rho_v}{\rho_l}(1-\alpha)\frac{\text{Min}\left(0, P - P_{vap}\right)}{0.5\rho_{ref}U_{ref}^2} + C_{des}\frac{\rho_v}{\rho_l}\alpha\frac{\text{Max}\left(0, P - P_{vap}\right)}{0.5\rho_{ref}U_{ref}^2} \tag{33}$$

where C_{prod}, C_{des} are constants to calibrate.

The evaluation of the pressure when cavitation appears is not clear using compressible solvers. We decided to set the pressure to its saturation value P_{vap} at the reference temperature. In this case, the production term is never activated. We introduced a parameter ε in order to be smaller than P_{vap}: $P = P_{vap} - \varepsilon$. In all our computations, ε was set to 10^{-3}. The influence of this parameter has not been studied.

14

Moreover, with this formulation, the void ratio value can be higher than one. We added a limiter in the solver to clip the void ratio into its physical domain of evolution.

This kind of model reproduces propagation of acoustic disturbance at the Wallis speed of sound that is not thermodynamically coherent. Moreover, the behaviour of the mixture entropy has never been studied.

4. Numerical methods

The conservation laws governing both models can be written in the form:

$$\frac{\partial w}{\partial t} + \frac{\partial F(w)}{\partial x} = S \tag{34}$$

where w is the vector of variables, F the convective flux and S the source term (only for the void ratio equation). The void ratio equation is written in its divergence form:

$$\frac{\partial \alpha}{\partial t} + \frac{\partial(\alpha u)}{\partial x} = (K + \alpha)\frac{\partial u}{\partial x} + \frac{\dot{m}}{\rho_I} \tag{35}$$

We focus herein on some finite volume schemes. Regular meshes are considered, whose size Δx is such that: $\Delta x = x_{i+1/2} - x_{i-1/2}$. Let us denote as usual Δt the time step, where $\Delta t = t^{n+1} - t^n$. Let w_i^n be the approximate value of $\frac{1}{\Delta x}\int_{x_{i-1/2}}^{x_{i+1/2}} w(x, t^n)dx$. A discrete form of equation (34) can be written as:

$$\Delta x \frac{w_i^{n+1} - w_i^n}{\Delta t} + F_{i+1/2}^n - F_{i-1/2}^n = S_i^n \Delta x \tag{36}$$

where $F_{i+1/2}^n$ is the numerical flux through the cell interface $x_{i+1/2} \times [t^n, t^{n+1}]$. The time step should comply with some CFL condition in order to guarantee

15

some stability requirement.

Various formulations of numerical flux have been proposed to solve multi-phase compressible flows. In the present study, we tested and compared various formulations: the Jameson-Schmidt-Turkel scheme [62], an AUSM-type scheme [34, 63, 64, 65], the Rusanov scheme [66], the HLLC scheme [67, 68, 69] and the VF Roe non conservative scheme [70, 71, 72]. The Jameson scheme is stabilized by an artificial viscosity, which includes a second-order and a fourth-order dissipation terms. Each term involves a tunable numerical coefficient, $k^{(2)}$ and $k^{(4)}$ respectively. To detect discontinuities a sensor based on pressure gradients is used. For two-phase flows, the sensor is also evaluated with density gradients.

The AUSM-type and VF Roe schemes are shortly described in Appendix C and D.

4.1. Treatment of the source term

The numerical simulations of the initial-boundary value problems are accomplished using splitting approach. One starts in solving the source-free homogeneous part of the whole system:

$$\frac{\partial w}{\partial t} + \frac{\partial F(w)}{\partial x} = 0 \tag{37}$$

This is followed by solving the system of ordinary differential equations describing the mass transfer between phases to obtain the complete solution:

$$\frac{dw}{dt} = S(w, \nabla w) \tag{38}$$

4.2. Inlet and outlet boundary conditions

The numerical treatment of the boundary conditions is based on the use of the characteristic relations of Euler equations. The number of variables to impose at boundaries is given by the number of positive characteristics. The characteristic relations obtained for the 5-equation system are (see Appendix A for the 4-equation system):

$$-c^2(\rho^c - \rho^s) + (P^c - P^s) = 0 \tag{39}$$

$$(P^c - P^s) + \rho c(V^c - V^s) = 0 \tag{40}$$

$$(P^c - P^s) - \rho c(V^c - V^s) = 0 \tag{41}$$

$$(Y^c - Y^s) = 0 \tag{42}$$

$$\rho(\alpha^c - \alpha^s) - K(\rho^c - \rho^s) = 0 \tag{43}$$

The variables with superscript c denote the variables to be computed at the boundary. Variables with superscript s denote the variables obtained by the current numerical scheme.

At inflow, we impose the initial values of the void ratio, densities of pure phases and the velocity. The pressure is evaluated with the relation (41) and all variables can be evaluated at the boundary.

At outflow, the static pressure is imposed. The variables are computed with four characteristic relations (39), (40),(42) and (43).

5. Presentation of the rarefaction test cases

5.1. Water-gas mixture expansion tube, $\mid u \mid= 2 \ m/s$

This test consists in a one meter long tube filled with liquid water at atmospheric pressure and with density $\rho_l =$1150 kg/m^3. The temperature of

water is $T = 355$ K. A weak volume fraction of vapor $\alpha =0.01$ is initially added to the liquid. The initial discontinuity is set at 0.5 m, the left velocity is -2 m/s and the right velocity is 2 m/s. The solution involves two expansion waves. As gas is present, the pressure cannot become negative. To maintain positive pressure, the gas volume fraction increases due to the gas mechanical expansion and creates a pocket. Liquid water is expanded until the saturation pressure is reached then evaporation appears and quite small amount of vapor is created. The solution with phase transition is composed of four expansion waves. The extra two expansion waves correspond to the evaporation fronts.

This test was computed with a 5-equation model in [10] and with a 7-equation model in [49]. The solution extracted from [49] using a 5000-cell mesh is presented in Fig. 1. The evolution of mass and volume fractions, the velocity and the pressure are plotted at time $t = 3.2$ ms.

5.2. Water-gas mixture expansion tube, $\mid u \mid= 100\ m/s$

The same conditions are used except regarding velocities which are set to u=-100 m/s on the left, and u=100 m/s on the right. In this case, evaporation is much more intense resulting in a large cavitation pocket where the gas volume fraction is close to 1. However, this pocket does not contain pure gas but a mixture at thermodynamic equilibrium.

The solution extracted from [49] using a 5000-cell mesh is presented in Fig. 2. The evolution of mass and volume fractions, the velocity and the pressure are plotted at time $t = 1.5$ ms.

6. Results and discussion

The numerical tool has been validated on two-phase shock-tube problems without phase transition (liquid-gas mixture and epoxy-spinel mixture as computed in [73, 9]). Results are not presented, we focus here on the cavitation cases.

The double rarefaction test case presented previously is considered for the validation. Two initial velocities are tested: $u = \pm 2$ m/s and $u = \pm 100$ m/s. Moreover, two values of the initial volume fraction of vapor are tested: $\alpha = 10^{-2}$ and $\alpha = 10^{-10}$. With the last value, quasi pure liquid is present initially and the three-equation model can be used.

A shock-cavitation interaction is also considered. It is the same expansion tube problem for which both extremities are closed leading to shock waves generation.

The parameters of the stiffened gas EOS and saturation values for densities are given in Table 2. The quantities have been evaluated with a saturation table at the reference temperature. The vapour pressure $P_{vap} = 51000$ Pa.

6.1. Study of cavitation models

6.1.1. Expansion tube with initial value $\alpha = 10^{-2}$

The mesh contains 5000 cells as used in [49]. The time step is set to 10^{-7} s. Various simulations were performed by varying the cavitation model (4- and 5-equation models) and the constant of models (c_{baro} and C_{prod}). The constant C_{des} is set to 0 because the case involves only an evaporation process. All computations were performed with the Rusanov scheme.

Calibration of c_{baro}

First, we present the influence of the constant c_{baro} for the low speed case $u = \pm 2$ m/s. Solutions are shown in Fig. 3 at time $t = 3.2$ ms. The void ratio profiles put in evidence the large influence of the constant c_{baro}. Greater is this constant, lower is the maximum value of the void ratio. In comparison with simulations presented in [11, 49], the better result is obtained with $c_{baro} = 1.31$ m/s. With this value, results are in very close agreement with the two-fluid solution. The same void ratio profiles are plotted with a logarithmic scale. We clearly observe the two rarefaction waves and the two evaporation fronts. The influence of c_{baro} is also well marked on the pressure evolution. Greater is this constant, greater is the non equilibrium effect on the pressure, as expected. The mixture speed of sound c is shown in this figure with a logarithmic scale. The jump of speed of sound across the four waves are well illustrated. At the ends of the tube, the speed of sound follows the Wallis formulation: $c = 80$ m/s. The minimal value is given by the constant c_{baro}.

The influence of the constant c_{baro} for the high speed case $u = \pm 100$ m/s is presented in Fig. 4, at time $t = 1.5$ ms. The influence is weak on both the volume and mass fractions, and the velocity evolution. For the pressure profiles, the non equilibrium effect is clearly visible. This phenomenon is very intense, it reaches 0.3 bar in the solution presented in [49]. In our simulations, it reaches only 0.05 bar, except with the highest value of c_{baro}. When $c_{baro} = 3.38$ m/s, the non equilibrium effect is important (0.2 bar) but centered on P_{vap} due to the symmetric form of the EOS. An improvement of the model should be done by building a non-symmetric barotropic EOS

or by using non isothermal model. The constant c_{baro} is set to 1.31 m/s, as previously.

Calibration of C_{prod}

The calibration of the constant C_{prod} is presented in Fig. 5 for the case $u = \pm 2$ m/s. The void ratio and mass fraction evolutions are illustrated. Greater is this constant, greater are the volume and mass fractions, as expected. We can calibrate the model with the reference simulations presented in [11, 49]. The closest result is obtained with $C_{prod} = 1$.

For the high speed case $u = \pm 100$ m/s, results are plotted in Fig. 6. The influence is weak on the void ratio profiles. Differences are marked on the mass fraction. A calibration can be done using the solution of Zein [49]. The better results is obtained with $C_{prod} = 100$, instead of 1 in the previous case. It is a characteristic of this model, the calibration varies with the test case. The mixture speed of sound is plotted in the same figure. For this quantity, we have not any reference solution. On both extremities of the tube, the speed of sound is around 80 m/s. When the cavitation pocket develops, the speed of sound first decreases around 20 m/s, and for void ratio values close to one, the speed of sound increases up to 300 m/s.

Models comparison

Computations have been done with the 5-equation model including the barotropic source term, with the constant $c_{baro} = 1.31$ m/s. All models are compared in Fig. 7 for the low speed case $u = \pm 2$ m/s. The 4- and 5-equation models provide an identical solution. Between the 4-equation models, the void ratio

21

profiles are quite similar. The mass fraction obtained with both models are close to those obtained in [11, 49]. The pressure evolution given by the empirical 4-equation model do not reproduce the pressure diminution across the evaporation fronts. Large discrepancies are noticeable on the mixture speed of sound evolution (plotted with a logarithmic scale). It is due to the fact that the empirical 4-equation model reproduces the Wallis speed of sound even when mass transfer is taken into account.

For the high speed case, all models are compared in Fig. 8. Solutions obtained with the 4- and 5-equation barotropic models are superposable. For the mass fraction profile, the maximum value provided by the 4-equation barotropic model is under-estimated in comparison with the solution of Zein [49] and with the solution given by the empirical 4-equation model. With this model, evaporation fronts can not be predicted on the pressure evolution. For the mixture speed of sound, large discrepancies are visible. With the barotropic speed of sound, we can clearly observe variations across the different waves.

6.1.2. Expansion tube with initial value $\alpha = 10^{-10}$

We consider the same test case but the initial gas fraction is now set to 10^{-10}. The barotropic 3-equation model can be compared with other models. For this test case, we have not any reference solutions, we just propose a qualitative comparison between models. The speed of sound is initially around 1400 m/s in the water. We performed computations on a 5000-cell mesh and compared solutions at time $t = 0.2$ ms. The time step is set to 10^{-8} s.

Calibration of c_{baro}

For both cases, the influence of c_{baro} is weak. It is illustrated in Fig. 9 for the high speed case. The influence on the void ratio is null and it is weak on the mass fraction. In comparison with the case with a small initial gas fraction, the maximum value of the mass fraction is twice as high. On the pressure evolution, the evaporation fronts are well illustrated. The non-monotonic behaviour of the mixture speed of sound is clearly observed. In the cavitation pocket where void ratio values are close to one, the speed of sound increases and tends to the pure gas sound speed. As previously, the same value $c_{baro} = 1.31$ m/s is kept.

Calibration of C_{prod}

The influence of the constant C_{prod} is illustrated in Fig. 10 on the volume and mass fractions for the low speed case. The maximum value increases when the constant increases. From $C_{prod} = 75$, results do not move any more. We calibrated the constant in order to obtain the maximum value of the mass fraction close to the previous case with the initial value $\alpha = 10^{-2}$, that is $c_{prod} = 10$.

The same quantities are plotted in Fig. 11 for the high speed case. From the value 10^6, the solution does not move any more. We decide to set C_{prod} to this value.

For the considered test cases, the domain of evolution of C_{prod} varies between 1 and 10^6. It is clearly a large drawback of the model.

Models comparison

The comparison with all models is shown in Fig. 12 for the low speed case. Computations were performed with the 3-, 4- and 5-equation models ($c_{baro} = 1.31$ m/s and $C_{prod} = 10$). As previously, solutions obtained with the 4- and 5-equation models with the barotropic source term are identical. The volume and mass fraction peaks mark differences between the 3- and 4-equation barotropic models. With the void ratio equation, the maximum value is 1.75 times higher for the void ratio and 3 times higher for the mass fraction. With respect to the width of the cavitation pocket, the solution provided by the empirical 4-equation model is larger in comparison with other models.

The evolution of the pressure is consistent with our expectations. A small non equilibrium effect and evaporation fronts are visible with all barotropic models.

The mixture speed of sound is plotted with a logarithmic scale for both 4-equation models. Large variations are highlighted, from the pure liquid high value to small values in the cavitation pocket. With the barotropic speed of sound, the four waves can be observed and the ratio between extremal sound velocities is higher than 1000.

For the high speed case $u = \pm100$ m/s, the 3-equation barotropic model was unable to provide a solution (all computations led to divergence). This model seems less robust than other barotropic models. All models are compared in fig. 13 ($c_{baro} = 1.31$ m/s and $C_{prod} = 10^6$). The 4- and 5-equation barotropic models give similar results. A large discrepancy appears on the mass fraction

between the two formulations of 4-equation model (almost a factor 9). The width of the evaporation area visible on the void ratio evolution is slightly higher with the empirical 4-equation model. The Wallis and barotropic speed of sound, plotted with a logarithmic scale, mark large differences, as expected.

6.2. Influence of the numerical scheme

The five numerical schemes were tested on the rarefaction cases with the initial velocity $u = \pm 2$ m/s and $u = \pm 100$ m/s. It was not possible to obtain a correct solution with the HLLC, VF Roe and AUSM schemes using the barotropic source term. All computations led to divergence or oscillating solutions. The approximate Riemann solvers (HLLC and VF Roe) are known to fail when very low densities and pressures near the vacuum appear. An anti-diffusive term can be added to the HLLC dissipation to improve the scheme [74, 75]. It has been not tested in the present study. Similarly, the AUSM-type formulation was not able to compute such applications.

Only the more dissipative schemes (Jameson and Rusanov) provided solutions for all cases. Using the second-order Jameson scheme, the dissipation parameter k_2 is set to 1 and k_4 varies between 0.008 and 0.02.

Comparisons between the Jameson and Rusanov schemes are presented in Fig. 14 using the barotropic 4-equation model in which the constant c_{baro} is set to 1.31 m/s. The considered test case is the expansion problem with the low speed $u = \pm 2$ m/s and $\alpha = 10^{-2}$. Results are very similar. Pressure and velocity evolutions are identical. A small discrepancy appears only on the void ratio maximum value.

With respect to the CPU time, it is 18.8h for the two-fluid computation [49],

whereas with our solver, using the 4-equation barotropic model, it is smaller than 5 minutes.

The same scheme comparison for the high speed case is presented in Fig. 15 for the void ratio and pressure profiles. Results are obtained with $c_{baro} = 1.31$ m/s. Solutions are quasi identical. With respect to the CPU time, it is 8.5h for the two-fluid computation [49], whereas with our solver it is smaller than 5 minutes.

6.3. Expansion tube with shock-cavitation interaction

This case is similar to the previous one, except that the two ends of the tube are simultaneously closed once the flow starts. Therefore, a shock created at each end moves towards the center, resulting in shock-cavitation interaction and cavitation collapse. The flow is initially quasi pure water and soon changes phase into a vapour-liquid mixture at the center, and then reverting back into a pure liquid after the cavitation collapse. A similar test case was depicted in [37] on a 400-cell mesh. Authors used a 3-equation solver with various EOS for the mixture and a HLL numerical scheme.

A uniform mesh of 5000 cells is used and the time step is set to 10^{-8} s. Various simulations are compared with the different models. Values for constants c_{baro} and C_{prod} are set to 1.31 m/s and 10^6 respectively. With the 3-equation model, all simulations led to divergence, as observed previously. Similarly, only the Rusanov and Jameson numerical schemes allowed to obtain results.

First, we studied the influence of the numerical scheme using the new 4-equation model. Volume and mass fractions obtained with both numerical

26

schemes are plotted at different times in Fig. 16 (with a logarithmic scale for the mass fraction). As the cavitation pocket grows, up to time $t = 0.3$ ms, solutions are similar to those presented in the previous case. Discrepancies between schemes are weak, a different form on the mass fraction profiles is noticeable. After time $t = 0.3$ ms, the shocks created at the ends meet the rarefaction waves generated at the center, and then interacts with the expanding cavitation interface. The cavitation collapse begins. Both simulations predict the decrease of the volume and mass fractions. With the Rusanov scheme, the phenomenon is more intense. At time $t = 0.7$ ms, the maximum void ratio value is close to 0.2, whereas the value obtained with the Jameson scheme is around 0.4. Mass fraction values are very small at this time: around 5.10^{-5} for the Rusanov scheme and 2.10^{-4} for the Jameson scheme. Moreover, oscillations on the solutions appear during the collapse. It is clearly visible at time $t = 0.45$ ms for both numerical schemes.

Secondly, the influence of the constant C_{des} is investigated for the Hosangadi model using the Rusanov scheme. As the condensation process is present in this case, the second constant C_{des} is no more null. Three values are tested: 0.1, 1 and 10. The influence of this constant is presented in Fig. 17 on the evolution of volume and mass fractions at different times. Both the growth and the decrease of the cavitation pocket are well illustrated. As expected, higher is the constant C_{des}, more intense is the condensation phenomenon. At time $t = 0.7$ ms, the maximum void ratio values are 0.5, 0.3, 10^{-9}, for C_{des}=0.1, 1, 10, respectively. Similarly to the previous computations, we observe numerical oscillations during the cavitation collapse, especially at time

$t = 0.45$ ms but also at time $t = 0.7$ ms.

The comparison between both 4-equation models is shown in Fig. 18 with pressure and density profiles at different times. The constant C_{des} is set to 1. The shock propagation through the rarefaction region is well illustrated on both the pressure and density profiles, up to time $t = 0.35$ ms. Both models provide similar results. Then shocks interacts with the expanding cavitation interface, resulting in a discontinuity forms at the interface. The cavitation collapse generates two shocks which propagate outwards. Oscillations on the density profiles during the cavitation collapse are clearly visible at time $t = 0.5$ ms with both models. At time $t = 0.6$ ms, discrepancies appear on the density profiles. The empirical 4-equation model provides a higher maximum void ratio value (see also the void ratio profiles in previous figures). In comparison with results presented in [37] computed with a 3-equation model, we observe large differences on the intensity of the shocks created during the cavitation collapse. In their simulations the two shocks propagates with equal strength as that for the shocks generated initially at the two ends. In our simulations, the strength of shocks is very lower: the maximum pressure is around 100 bars at time $t = 0.5$ ms instead of 1700 bars for the initial shocks.

7. Conclusion

In the present study, a comparison of models was proposed for the simulation of 1D inviscid cavitating flows. A hierarchy of homogeneous model from 3 to 5 equations was investigated. The 3-equation model was closed with a sinusoidal barotropic EOS. A new source term based on barotropic EOS prop-

erties was introduced for a 4- and 5-equation model. Moreover, a 4-equation model with an empirical source term involving evaporation and condensation processes was studied. The proposed models were validated through various test-cases based on rarefaction waves leading to a phase transition, for which numerical solutions obtained with 2-fluid models are available. A shock-cavitation interaction case was also considered. The capability to obtain correct solutions for rarefaction waves, evaporation fronts and cavitation collapse has been investigated. These test-cases lead to different concluding remark:

- The 4- and 5-equation models provided identical solutions. It seems that it is not necessary to allow the liquid to be in a metastable state.

- Between the 3- and 4-equation models built with the barotropic EOS, large discrepancies appeared for the prediction of both the volume and mass fractions. For the stiffest cases, the 3-equation model was unable to give a solution. On the contrary, the 4-equation model showed good properties of robustness and provided a good quality of solutions while initial velocities are moderate.

- Solutions obtained with the two formulations of 4-equation models marks large differences for the mass and volume fraction (both the maximum values and the width of the cavitation pocket), for the stiffest cases. Moreover, the non equilibrium effect on the pressure can not be reproduced by the empirical model. With respect to the constant calibration, the parameter c_{baro} was easy to calibrate. All computations were performed with one fixed value. On the contrary, the constant

C_{prod} varies largely between cases (from 1 to 10^6). The calibration of this model is a real problem.

On another hand, a comparison of various numerical schemes was proposed. Different families were considered: AUSM-family, approximate Riemann solvers (VF Roe, HLLC), a simple Godunov approach (Rusanov) and a space-centered scheme with artificial dissipation (Jameson). The simulation of rarefaction waves near the vacuum apparition was a hard case for both the approximate Riemann solvers and the AUSM scheme. It was not possible to obtain a solution with these schemes using the barotropic source term. Only the Jameson and Rusanov schemes allowed to simulate the cavitation cases. Finally, the proposed numerical tool allowed to drastically reduce the CPU cost in comparison with a 2-fluid model involving relaxation procedures for the pressure and the velocity.

Further works are in progress to introduce a non isothermal thermodynamic path and to perform realistic turbulent configurations.

Appendix

Appendix A: eigenvectors and characteristic relations, 4-equation model

The system written with primitive variables ${}^t W = (\alpha, P, u, e)$ is

$$
\frac{\partial}{\partial t}
\begin{pmatrix} \alpha \\ P \\ u \\ e \end{pmatrix}
+
\begin{bmatrix}
u & 0 & -K & 0 \\
0 & u & \rho c^2 & 0 \\
0 & 1/\rho & u & 0 \\
0 & 0 & P/\rho & u
\end{bmatrix}
\frac{\partial}{\partial x}
\begin{pmatrix} \alpha \\ P \\ u \\ e \end{pmatrix}
= 0
$$

Eigenvalues are $(u, u, u - c, u + c)$ and the associated right eigenvectors are

$$
R_1 = \begin{pmatrix} 0 \\ 0 \\ 0 \\ 1 \end{pmatrix}
\quad
R_2 = \begin{pmatrix} 1 \\ 0 \\ 0 \\ 0 \end{pmatrix}
\quad
R_3 = \begin{pmatrix} -\dfrac{K\rho}{P} \\[2mm] \dfrac{\rho^2 c^2}{P} \\[2mm] -\dfrac{\rho c}{P} \\[2mm] 1 \end{pmatrix}
\quad
R_4 = \begin{pmatrix} -\dfrac{K\rho}{P} \\[2mm] \dfrac{\rho^2 c^2}{P} \\[2mm] \dfrac{\rho c}{P} \\[2mm] 1 \end{pmatrix}
$$

And the left eigenvectors are

$$
{}^t L_1 = \begin{pmatrix} 0 \\ -\dfrac{P}{\rho^2 c^2} \\[2mm] 0 \\ 1 \end{pmatrix}
\quad
{}^t L_2 = \begin{pmatrix} 1 \\ \dfrac{K}{\rho c^2} \\[2mm] 0 \\ 0 \end{pmatrix}
\quad
{}^t L_3 = \begin{pmatrix} 0 \\ \dfrac{P}{2\rho^2 c^2} \\[2mm] -\dfrac{P}{2\rho c} \\[2mm] 0 \end{pmatrix}
\quad
{}^t L_4 = \begin{pmatrix} 0 \\ \dfrac{P}{2\rho^2 c^2} \\[2mm] \dfrac{P}{2\rho c} \\[2mm] 0 \end{pmatrix}
$$

Characteristic relations are given by

$$
{}^t L_i \left(\frac{\partial W}{\partial t} + A \frac{\partial W}{\partial x} \right) = 0 \tag{44}
$$

Finally, relations are

$$
\frac{dP}{dt} - c^2 \frac{d\rho}{dt} = 0 \tag{45}
$$

$$
\frac{d\alpha}{dt} - \frac{K}{\rho} \frac{d\rho}{dt} = 0 \tag{46}
$$

$$
\frac{dP}{dt} - \rho c \frac{du}{dt} = 0 \tag{47}
$$

$$
\frac{dP}{dt} + \rho c \frac{du}{dt} = 0 \tag{48}
$$

Appendix B: pressure equation

From the conservation laws for the mass of each phases, we have

$$
\frac{d\rho_v}{dt} = \frac{1}{\alpha} \left(\dot{m} - \rho_v \frac{d\alpha}{dt} \right) - \rho_v \frac{\partial u}{\partial x} \tag{49}
$$

31

$$\frac{d\,\rho_l}{d\,t} \;\; = \;\; \frac{1}{1-\alpha}\left(-\dot{m} + \rho_l \frac{d\,\alpha}{d\,t}\right) - \rho_l \frac{\partial u}{\partial x} \tag{50}$$

We deduce the following relation using the void ratio equation

$$\frac{1}{c_v^2}\frac{d\,P}{d\,t} \;\; = \;\; \frac{d\,\rho_v}{d\,t} \;\; = \;\; \frac{\dot{m}}{\alpha} - \frac{\rho_v}{\alpha}\left(K\frac{\partial u}{\partial x} + \frac{\dot{m}}{\rho_I}\right) - \rho_v \frac{\partial u}{\partial x} \tag{51}$$

The pressure equation is therefore

$$\frac{\partial P}{\partial t} + u\frac{\partial P}{\partial x} = -\rho_v c_v^2\left(1 + \frac{K}{\alpha}\right)\frac{\partial u}{\partial x} + \frac{c_v^2}{\alpha}\left(1 - \frac{\rho_v}{\rho_I}\right)\dot{m} \tag{52}$$

We introduce the Wallis speed of sound

$$\rho_v c_v^2\left(1 + \frac{K}{\alpha}\right) \;\; = \;\; \rho c_{wallis}^2 \tag{53}$$

Finally the expression of the pressure equation is

$$\frac{\partial P}{\partial t} + u\frac{\partial P}{\partial x} + \rho c_{wallis}^2 \frac{\partial u}{\partial x} = \frac{c_v^2}{\alpha}(1 - \frac{\rho_v}{\rho_I})\dot{m} \tag{54}$$

Appendix C: an AUSM-type scheme

The flux formulas of AUSM-type have been tested in the resolution of shock waves and interfaces in multicomponent problems under high density ratio between two phases [34, 63, 64, 65]. We proposed an AUSM+type formulation following the AUSM+up model proposed by Chang and Liou [65].

We define the interface speed of sound and the interface density as:

$$c_{1/2} \;\; = \;\; \frac{1}{2}(c_L + c_R) \qquad \text{and} \qquad \rho_{1/2} \;\; = \;\; \frac{1}{2}(\rho_L + \rho_R) \tag{55}$$

where subscripts L and R denote the left and right states with respect to the interface. The left and right Mach numbers are then defined based on this speed of sound as:

$$M_L \;\; = \;\; \frac{u_L}{c_{1/2}} \qquad \text{and} \qquad M_R \;\; = \;\; \frac{u_R}{c_{1/2}} \tag{56}$$

Then the following split Mach numbers and pressures are used, in which three sets of polynomials are required:

$$M_{(1)}^{\pm} = \frac{1}{2}(M \pm \mid M \mid) \tag{57}$$

$$M_{(4)}^{\pm} = \begin{cases} \pm\frac{1}{4}(M \pm 1)^2(1 + \frac{1}{2}(M \mp 1)^2) & \text{if} \qquad |M| < 1 \\ M_{(1)}^{\pm} & \text{otherwise} \end{cases} \tag{58}$$

And

$$P_{(5)}^{\pm} = \begin{cases} \frac{1}{4}(M \pm 1)^2(2 \mp M) \pm \frac{3}{16}M(M^2 - 1)^2 & \text{if} \qquad |M| < 1 \\ \dfrac{M_1^{\pm}}{M} & \text{otherwise} \end{cases} \tag{59}$$

The numerals in the subscripts of M and P indicate the degree of the polynomials. The interface values for Mach number and pressure are defined as:

$$M_{1/2} = M_{(4)}^+(M_L) + M_{(4)}^-(M_R)$$

$$P_{1/2} = P_{(5)}^+(M_L)P_L + P_{(5)}^-(M_R)P_R + K_u P_{(5)}^+(M_L)P_{(5)}^-(M_R)\rho_{1/2}c_{1/2}(u_L - u_R)$$

where K_u is a coefficient set to 0.125.

A general form of interface mass flux in the AUSM-type scheme is defined as:

$$(\rho u)_{1/2} = c_{1/2}\left(\rho_L M_{(1)}^+(M_{1/2}) + \rho_R M_{(1)}^-(M_{1/2})\right) + Dp \tag{60}$$

33

where Dp is a dissipation term based on pressure difference:

$$Dp = K_p \frac{\Delta M \operatorname{Max}(1 - \overline{M}^2, 0)(P_L - P_R)}{c_{1/2}} \tag{61}$$

$$\Delta M = M_{(4)}^+(M_L) - M_{(1)}^+(M_L) - M_{(4)}^-(M_R) + M_{(1)}^+(M_L) \tag{62}$$

$$\overline{M} = \frac{1}{2}(M_L + M_R) \tag{63}$$

where K_p is a coefficient set to 1.

For the void ratio equation, we introduce the interface velocity:

$$u_{1/2} = c_{1/2}\left(M_{(1)}^+(M_{1/2}) + M_{(1)}^-(M_{1/2})\right) \tag{64}$$

With the 4-equation system, the expression of the numerical flux is:

$$F_{i+1/2} = \begin{pmatrix} (\rho u)_{1/2} \\ \frac{1}{2}(\rho u)_{1/2}(u_L + u_R) - \frac{1}{2} \mid (\rho u)_{1/2} \mid (u_R - u_L) + P_{1/2} \\ \frac{1}{2}(\rho u)_{1/2}(H_L + H_R) - \frac{1}{2} \mid (\rho u)_{1/2} \mid (H_R - H_L) \\ \frac{1}{2}u_{1/2}(\alpha_L + \alpha_R) - \frac{1}{2} \mid u_{1/2} \mid (\alpha_R - \alpha_L) \end{pmatrix}$$

And with the 5-equation system:

$$F_{i+1/2} = \begin{pmatrix} \frac{1}{2}u_{1/2}(\alpha_{l_L}\rho_{l_L} + \alpha_{l_R}\rho_{l_R}) - \frac{1}{2} \mid u_{1/2} \mid (\alpha_{l_L}\rho_{l_L} - \alpha_{l_R}\rho_{l_R}) \\ \frac{1}{2}u_{1/2}(\alpha_{v_L}\rho_{v_L} + \alpha_{v_R}\rho_{v_R}) - \frac{1}{2} \mid u_{1/2} \mid (\alpha_{v_L}\rho_{v_L} - \alpha_{v_R}\rho_{v_R}) \\ \frac{1}{2}(\rho u)_{1/2}(u_L + u_R) - \frac{1}{2} \mid (\rho u)_{1/2} \mid (u_R - u_L) + P_{1/2} \\ \frac{1}{2}(\rho u)_{1/2}(H_L + H_R) - \frac{1}{2} \mid (\rho u)_{1/2} \mid (H_R - H_L) \\ \frac{1}{2}u_{1/2}(\alpha_L + \alpha_R) - \frac{1}{2} \mid u_{1/2} \mid (\alpha_R - \alpha_L) \end{pmatrix}$$

Appendix D: a VFRoe ncv scheme

The VFRoe non conservative scheme is an approximate Riemann solver introduced in [70, 71, 72]. Finding a matrix satisfying Roe's condition may be

difficult for two-phase problems with complex EOS. This fact has motivated the development of an alternative to the Roe scheme. The scheme is based on the resolution of linearized Riemann problems written in non conservative variables. It admits entropy-violating stationary discontinuities, we switch on the Rusanov scheme in this case.

Considering the change of variables $w \rightarrow W(w)$, the system reads in non conservative form:

$$\frac{\partial W}{\partial t} + B(W)\frac{\partial Y}{\partial x} = 0 \qquad (65)$$

where B is the matrix of the transformed system.

At each interface, we solve the following linearized Riemann problem:

$$\frac{\partial W}{\partial t} + B(\tilde{W})\frac{\partial W}{\partial x} = 0 \quad \text{with} \begin{cases} W(x,0) = W_L & \text{if} \quad x < 0 \\ W(x,0) = W_R & \text{if} \quad x > 0 \end{cases} \qquad (66)$$

where $\tilde{W}$ is an average state depending on W_L and W_R; here we use the simple arithmetic average. The matrix $B(\tilde{W})$ is diagonalizable with real eigenvalues $\tilde{\lambda}_i$. We note $\tilde{r}_i$ and $\tilde{l}_i$ the right and left eigenvectors respectively. The difference $W_R - W_L$ is projected directly into the space spanned by a linear combination of the right eigenvectors:

$$W_R - W_L = \sum_{i=1}^{p} \tilde{\alpha}_i \tilde{r}_i \qquad \text{with} \qquad \tilde{\alpha}_i = {}^t\tilde{l}_i.(W_R - W_L) \qquad (67)$$

The solution of the Riemann problem is composed of constant states sepa-

rated by a fan of p characteristic lines:

$$W(\frac{x}{t}; W_L, W_R) = \begin{cases} W_L & \text{if} \quad x < \tilde{\lambda}_1 t \\ W_k = W_L + \sum_{i=1}^{k} \tilde{\alpha}_i \tilde{r}_i & \text{if} \quad \tilde{\lambda}_k t < x < \tilde{\lambda}_{k+1} t \\ W_R & \text{if} \quad x > \tilde{\lambda}_p t \end{cases} \quad (68)$$

If we suppose that no eigenvalue vanishes, we note W^* the approximate state at the interface, i.e. for $\frac{x}{t} = 0$. The numerical flux is given by:

$$F_{i+1/2} = F(w(W^*)) \quad (69)$$

For the 4-equation model, we choose for the non conservative variable $^tW = (\tau, u, P, Y)$ where $\tau = \dfrac{1}{\rho}$ and $Y = \dfrac{\alpha \rho_v}{\rho}$ is the mass fraction. The matrix B can be easily computed:

$$B = \begin{bmatrix} u & -\tau & 0 & 0 \\ 0 & u & \tau & 0 \\ 0 & \rho c^2 & u & 0 \\ 0 & 0 & 0 & u \end{bmatrix} \quad (70)$$

The associated right eigenvectors are:

$$\tilde{r}_1 = \begin{pmatrix} \tilde{\tau} \\ \tilde{c} \\ \text{-}\tilde{\rho}\tilde{c}^2 \\ 0 \end{pmatrix} \quad \tilde{r}_2 = \begin{pmatrix} 1 \\ 0 \\ 0 \\ 0 \end{pmatrix} \quad \tilde{r}_3 = \begin{pmatrix} 0 \\ 0 \\ 0 \\ 1 \end{pmatrix} \quad \tilde{r}_4 = \begin{pmatrix} \tilde{\tau} \\ -\tilde{c} \\ \text{-}\tilde{\rho}\tilde{c}^2 \\ 0 \end{pmatrix}$$

And the left eigenvectors:

$$^t\tilde{l}_1 = \begin{pmatrix} 0 \\ \dfrac{1}{2\tilde{c}} \\ -\dfrac{\tilde{\tau}}{2\tilde{c}^2} \\ 0 \end{pmatrix} \quad ^t\tilde{l}_2 = \begin{pmatrix} 1 \\ 0 \\ \dfrac{\tilde{\tau}}{2\tilde{c}^2} \\ 0 \end{pmatrix} \quad ^t\tilde{l}_3 = \begin{pmatrix} 0 \\ 0 \\ 0 \\ 1 \end{pmatrix} \quad ^t\tilde{l}_4 = \begin{pmatrix} 0 \\ -\dfrac{1}{2\tilde{c}} \\ -\dfrac{\tilde{\tau}}{2\tilde{c}^2} \\ 0 \end{pmatrix}$$

36

For the 5-equation model, we use the non conservative variable ${}^tW = (s_1, s_2, u, P, Y)$ as proposed in [73], where s_k is the entropy of the phase k.

References

[1] Baer M, Nunziato J. A two-phase mixture theory for the deflagration-to-detonation transition (DDT) in reactive granular materials. Int Journal of Multiphase Flow 1986;12:861–89.

[2] Saurel R, Metayer OL. A multiphase model for compressible flows with interfaces, shocks, detonation waves and cavitation. Journal of Fluid Mechanics 2001;431:239–71.

[3] Metayer OL, Massoni J, Saurel R. Modelling evaporation fronts with reactive Riemann solvers. Journal of Computational Physics 2005;205(2):567–610.

[4] Yeom G, Chang K. Numerical simulation of two-fluid two-phase flows by HLL scheme using an approximate jacobian matrix. Numerical Heat Transfer, Part B 2006;49:155–77.

[5] Yeom G, Chang K. Flux base wave decomposition scheme for an isentropic hyperbolic two-fluid model. Numerical Heat Transfer, Part B 2011;59:288–318.

[6] Mimouni S, Archer A, Laviville J, Boucker M, Mchitoua N. Modelling and computation of unsteady cavitation flows. La Houille Blanche 2006;6:121–8.

[7] Mimouni S, Boucker M, Lavieville J, Guelfi A, Bestion D. Modelling and computation of cavitation and boiling bubbly flows with Neptune CFD code. Nuclear Engineering and Design 2008;238:680–92.

[8] Kapila A, Menikoff R, Bdzil J, Son S, Stewart D. Two-phase modeling of deflagration-to-detonation transition in granular materials: reduced equations. Physics of fluids 2001;13(10):3002–24.

[9] Petitpas F, Franquet E, Saurel R, Metayer OL. A relaxation-projection method for compressible flows. Part II: artificial heat exchanges for multiphase shocks. Journal of Computational Physics 2007;225(2):2214–48.

[10] Saurel R, Petitpas F, Abgrall R. Modelling phase transition in metastable liquids: application to cavitating and flashing flows. Journal of Fluid Mechanics 2008;607:313–50.

[11] Saurel R, Petitpas F, Berry A. Simple and efficient relaxation methods for interfaces separating compressible fluids, cavitating flows and shocks in multiphase mixtures. Journal of Computational Physics 2009;228(5):1678–712.

[12] Allaire G, Clerc S, Kokh S. A five-equation model for the simulation of interfaces between compressible fluids. Journal of Computational Physics 2002;181(2):577–616.

[13] Kreeft J, Koren B. A new formulation of Kapila's five-equation model for compressible two-fluid flow, and its numerical treatment. Journal of Computational Physics 2010;229(18):6220–42.

[14] Tian B, Toro E, Castro C. A path-conservative method for a five-equation model of two-phase flow with an HLLC-type Riemann solver. Computers & Fluids 2011;46(1):122–32.

[15] Guillard H, Labois M. Numerical modelling of compressible two-phase flows. In: ECCOMAS CFD 2006, The Netherlands. http://proceedings.fyper.com/eccomascfd2006. 2006,.

[16] Merkle C, Feng J, Buelow P. Computation modeling of the dynamics of sheet cavitation. In: 3rd International Symposium on Cavitation CAV1998, Grenoble, France. 1998,.

[17] Kunz R, Boger D, Stinebring D, Chyczewski T, Lindau J, Gibeling H, et al. A preconditioned Navier-Stokes method for two-phase flows with application to cavitation prediction. Computers & Fluids 2000;29(8):849–75.

[18] Senocak I, Shyy W. A pressure-based method for turbulent cavitating flow computations. Journal of Computational Physics 2002;176(2):363–83.

[19] Singhal A, Athavale M, Li H, Jiang Y. Mathematical basis and validation of the full cavitation model. Journal of Fluids Engineering 2002;124(3):617–24.

[20] Venkateswaran S, Lindau J, Kunz R, Merkle C. Computation of multiphase mixture flows with compressibility effects. Journal of Computational Physics 2002;180(1):54–77.

[21] Vortmann C, Schnerr G, Seelecke S. Thermodynamic modeling and simulation of cavitating nozzle flow. Int Journal of Heat and Fluid Flow 2003;24:774–83.

[22] Hosangadi A, Ahuja V. Numerical study of cavitation in cryogenic fluids. Journal of Fluids Engineering 2005;127(2):267–81.

[23] Utturkar Y, Wu J, Wang G, Shyy W. Recent progress in modelling of cryogenic cavitation for liquid rocket propulsion. Progress in Aerospace Sciences 2005;41:558–608.

[24] Wu J, Wang G, Shyy W. Time-dependent turbulent cavitating flow computations with interfacial transport and filter-based models. Int Journal for Numerical Methods in Fluids 2005;49(7):739–61.

[25] Zhang X, Qiu L, Gao Y, Zhang X. Computational fluid dynamic study on cavitation in liquid nitrogen. Cryogenics 2008;48:432–8.

[26] Downar-Zapolski P, Bilicki Z, Bolle L, Franco J. The non-equilibrium relaxation model for one-dimensional flashing liquid flow. Int Journal of Multiphase Flow 1996;22(3):473–83.

[27] Bilicki Z, Kwidzinski R, Mohammadein S. Evaluation of the relaxation time of heat and mass exchange in the liquid-vapour bubble flow. Int Journal of Heat and Mass Transfer 1996;39(4):753–9.

[28] Barret M, Faucher E, Herard J. Schemes to compute unsteady flashing flows. AIAA Journal 2002;40(5):905–13.

[29] Helluy P, Seguin N. Relaxation models of phase transition flows. Mathematical Modelling and Numerical Analysis 2006;40(2):331–52.

[30] Delannoy Y, Kueny J. Two phase flow approach in unsteady cavitation

modelling. In: Cavitation and Multiphase Flow Forum, ASME-FED, vol. 98, pp.153-158. 1990,.

[31] Saurel R, Abgrall R. A simple method for compressible multifluid flows. SIAM Journal of Scientific Computing 1999;21(3):1115–45.

[32] Schmidt D, Rutland C, Corradini M. A fully compressible, two-dimensional model of small, high-speed, cavitating nozzles. Atomization and Sprays 1999;9:255–76.

[33] Clerc S. Numerical simulation of the homogeneous equilibrium model for two-phase flows. Journal of Computational Physics 2000;161(1):354–75.

[34] Edwards J, Franklin R. Low-diffusion flux splitting methods for real fluid flows with phase transition. AIAA Journal 2000;38(9):1624–33.

[35] Ventikos Y, Tzabiras G. A numerical method for the simulation of steady and unsteady cavitating flows. Computers & Fluids 2000;29(1):63–88.

[36] Shin B, Iwata Y, Ikohagi T. Numerical simulation of unsteady cavitating flows using a homogeneous equilibrium model. Computational Mechanics 2003;30:388–95.

[37] Liu T, Khoo B, Xie W. Isentropic one-fluid modelling of unsteady cavitating flow. Journal of Computational Physics 2004;201(1):80–108.

[38] Moreau J, Simonin O, Habchi C. A numerical study of cavitation influence on diesel jet atomisation. In: 19th annual meeting of the institute for liquid atomization and spray systems, Notthingham, England. 2004,.

[39] Vuyst FD, Ghidaglia J, Coq GL. On the numerical simulation of multiphase water flows with changes of phase and strong gradients using the Homogeneous Equilibrium Model. Int Journal on Finite Volumes 2005;2(1):1–36.

[40] Schmidt S, Sezal I, Schnerr G. Compressible simulation of high-speed hydrodynamics with phase change. In: European Conference on Computational Fluid Dynamics ECCOMAS 2006, Delft, The Netherlands. 2006,.

[41] Sinibaldi E, Beux F, Salvetti M. A numerical method for 3D barotropic flows in turbomachinery. Flow Turbulence Combustion 2006;76:371–81.

[42] Ihm S, Kim C. Computations of homogeneous-equilibrium two-phase flows with accurate and efficient shock-stable schemes. AIAA Journal 2008;46(12):3012–37.

[43] Goncalves E, Patella RF. Numerical simulation of cavitating flows with homogeneous models. Computers & Fluids 2009;38(9):1682–96.

[44] Goncalves E, Patella RF. Numerical study of cavitating flows with thermodynamic effect. Computers & Fluids 2010;39(1):99–113.

[45] Hu Z, Dou H, Khoo B. On the modified dispersion-controlled dissipative (DCD) scheme for computation of flow supercavitation. Computers & Fluids 2011;40(1):315–23.

[46] Barberon T, Helluy P. Finite volume simulation of cavitating flows. Computers & Fluids 2005;34(7):832–58.

[47] Faccanoni G, Kokh S, Allaire G. Modelling and simulation of liquid-vapor phase transition in compressible flows based on thermodynamical equilibrium. Math Modelling and Numerical Analysis 2012;(46):1029–54.

[48] Abgrall R. How to prevent pressure oscillations in multicomponent flow calculations : a quasi conservative approach. Journal of Computational Physics 1996;125(1):150–60.

[49] Zein A, Hantke M, Warnecke G. Modeling phase transition for compressible two-phase flows applied to metastable liquids. Journal of Computational Physics 2010;229(8):2964–98.

[50] Neaves M, Edwards J. All-speed time-accurate underwater projectile calculations using a preconditioning algorithm. Journal of Fluid Eng 2006;128(3):284–96.

[51] Rolland J, Patella RF, Goncalves E, Boitel G, Barre S. Experiments and modelling of cavitating flows in venturi. Part I: stable cavitation. In: 6th International Symposium on Cavitation CAV2006, Wageningen, The Netherlands. 2006,.

[52] Housman J, Kiris C, Hahez M. Preconditioned methods for simulations of low speed compressible flows. Computers & Fluids 2009;38(7):1411–23.

[53] Kinzel M, Lindau J, Kunz R. An examination of thermal modeling affects on the numerical prediction of large-scale cavitating fluid flows.

44

In: 7th International Symposium on Cavitation CAV2009, Ann Arbor, USA. 2009,.

[54] Bilanceri M, Beux F, Salvetti M. Investigation on numerical schemes in the simulation of barotropic cavitating flows. In: 7th International Symposium on Cavitation CAV2009, Ann Arbor, USA. 2009,.

[55] Goncalves E. Numerical study of unsteady turbulent cavitating flows. European Journal of Mechanics B/Fluids 2011;30(1):26–40.

[56] Goncalves E, Decaix J. Wall model and mesh influence study for partial cavities. European Journal of Mechanics B/Fluids 2012;31(1):12–29.

[57] Ishii C, Hibiki T. Thermo-fluid dynamics of two-phase flow. Springer; 2006.

[58] Metayer OL, Massoni J, Saurel R. Elaborating equations of state of a liquid and its vapor for two-phase flow models. Int Journal of Thermal Sciences 2004;43:265–76.

[59] Wallis G. One-dimensional two-phase flow. New York: McGraw-Hill; 1967.

[60] Petitpas F, Massoni J, Saurel R, Lapedie E, Munier L. Diffuse interface model for high speed cavitating underwater systems. Int Journal of Multiphase Flow 2009;35:747–59.

[61] Goncalves E, Patella RF. Constraints on equation of state for cavitating flows with thermodynamic effects. Applied Math and Computation 2011;217:5095–102.

[62] Jameson A, Schmidt W, Turkel E. Numerical solution of the Euler equations by finite volume methods using Runge-Kutta time stepping schemes. In: AIAA Paper 81–1259. 1981,.

[63] Paillere H, Corre C, Cascales JG. On the extension of the AUSM+ scheme to compressible two-fluid models. Computers & Fluids 2003;32(6):891–916.

[64] Niu Y, Lin Y, Lin Y. A simple and robust advection upwind fluw splitting to simulate transient cavitated water-vapor flows. Numerical Heat Transfer, Part A 2007;51:679–96.

[65] Chang C, Liou M. A robust and accurate approach to computing compressible multiphase flow: stratified flow model and AUSM+-up scheme. Journal of Computational Physics 2007;225(1):840–73.

[66] Rusanov V. Calculation of interaction of non-steady shock waves with obstacles. Journal of Computational Mathematics and Physics 1961;1:267–79.

[67] Toro E, Spruce M, Speares W. Restoration of the contact surface in the HLL-riemann solver. Shock Waves 1994;4:25–34.

[68] Batten P, Clarke N, Lambert C, Causon D. On the choice of wave speeds for the HLLC Riemann solver. SIAM J Sci Comput 1997;18(6):1553–70.

[69] Toro E. Riemann solvers and numerical methods for fluid dynamics. 2nd edition, New York: Springer; 1999.

[70] Buffard T, Gallouet T, Herard J. A sequel to a rough Godunov scheme: application to real gases. Computers & Fluids 2000;29(7):813–47.

[71] Gallouet T, Herard J, Seguin N. A hybrid scheme to compute contact discontinuities in Euler systems. Mathematical Modelling and Numerical Analysis 2002;36(6):1133–59.

[72] Gallouet T, Herard J, Seguin N. Some recent finite volume schemes to compuite Euler equations using real gas EOS. Int Journal for Numerical Methods in Fluids 2002;39:1073–138.

[73] Murrone A, Guillard H. A five equation reduced model for compressible two phase flows problems. Journal of Computational Physics 2005;202(2):664–98.

[74] Park S, Kwon J. On the dissipation mechanism of Godunov-type schemes. Journal of Computational Physics 2003;188(2):524–42.

[75] Bilanceri M, Beux F, Salvetti M. An implicit low-diffusive hll scheme with complete time linearization: application to cavitating barotropic flows. Computers & Fluids 2010;39:1990–2006.

Table 1: Thermodynamic assumptions and characteristics of models

models	5-eqt Kapila	5-eqt baro	4-eqt baro	3-eqt baro	HEM
solved	2 masses	2 masses	1 mass	1 mass	1 mass
equations	1 moment.	1 moment.	1 moment.	1 moment.	1 moment.
	1 energy	1 energy	1 energy	1 energy	1 energy
	$+ \alpha$	$+\alpha$	$+\alpha$		
equilibrium u	yes	yes	yes	yes	yes
equilibrium P	yes	1 pressure, non equilibrium effect			yes
equilibrium T	no	yes	yes	yes	yes
equilibrium g	no	no	no	no	yes
metastable	liquid	liquid	-	-	-
states	vapour	vapour	vapour	-	-

Table 2: Parameters of the stiffened gas EOS for water at $T = 355$K.

	γ	P_∞ (Pa)	q (J/kg)	C_p (J/K.kg)	ρ_{sat} (kg/m^3)
liquid	2.35	10^9	-0.1167 10^7	4267	1149.9
vapor	1.43	0	0.2030 10^7	1487	0.31
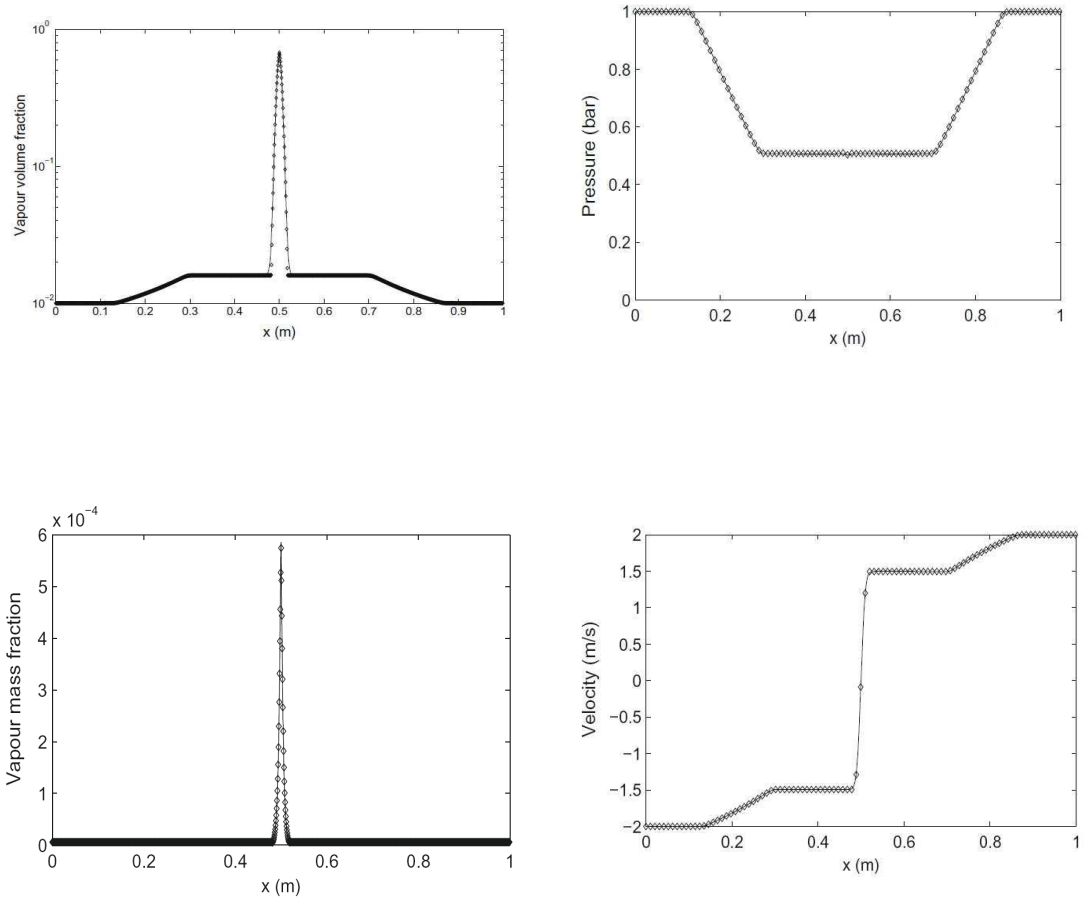
Figure 1: Water-gas double rarefaction with cavitation $|u| = 2$ m/s, solutions extracted from [49], mesh 5000 cells, $t = 3.2$ms. Volume and mass vapor fractions, pressure and velocity.
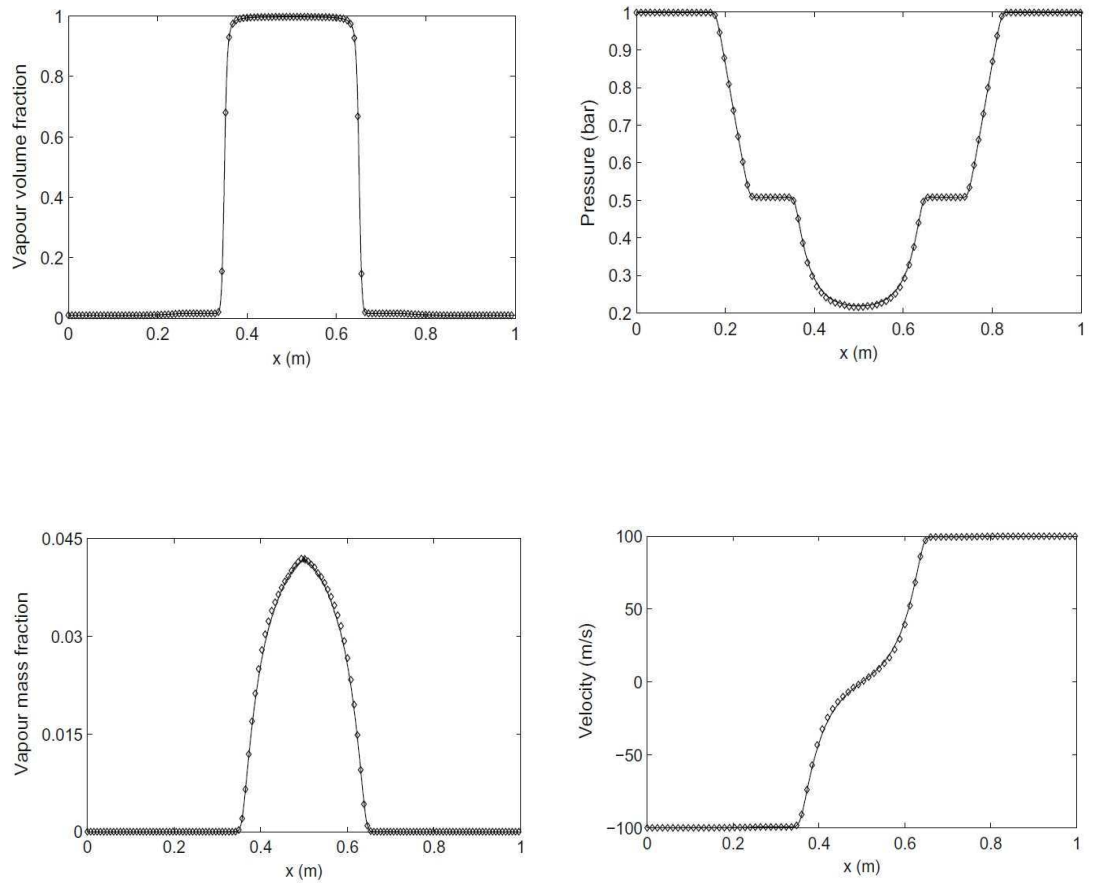
Figure 2: Water-gas double rarefaction with cavitation $|u| = 100$ m/s, solutions extracted from [49], mesh 5000 cells, $t = 1.5$ms. Volume and mass vapor fractions, pressure and velocity.
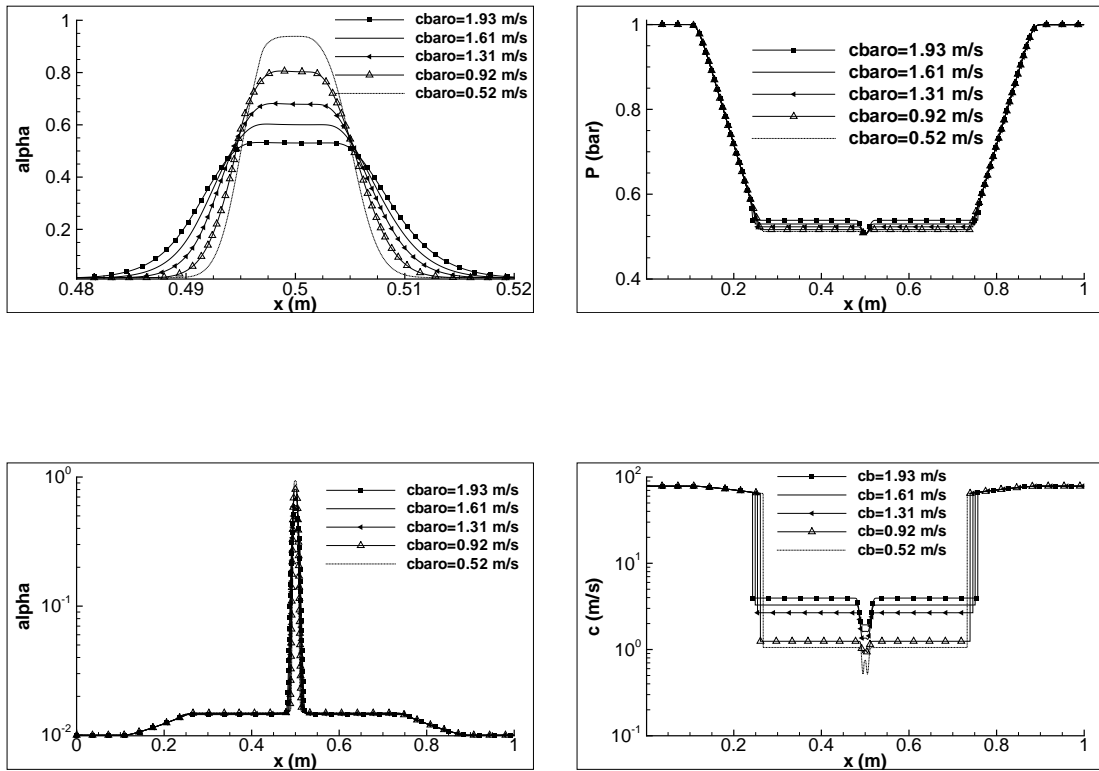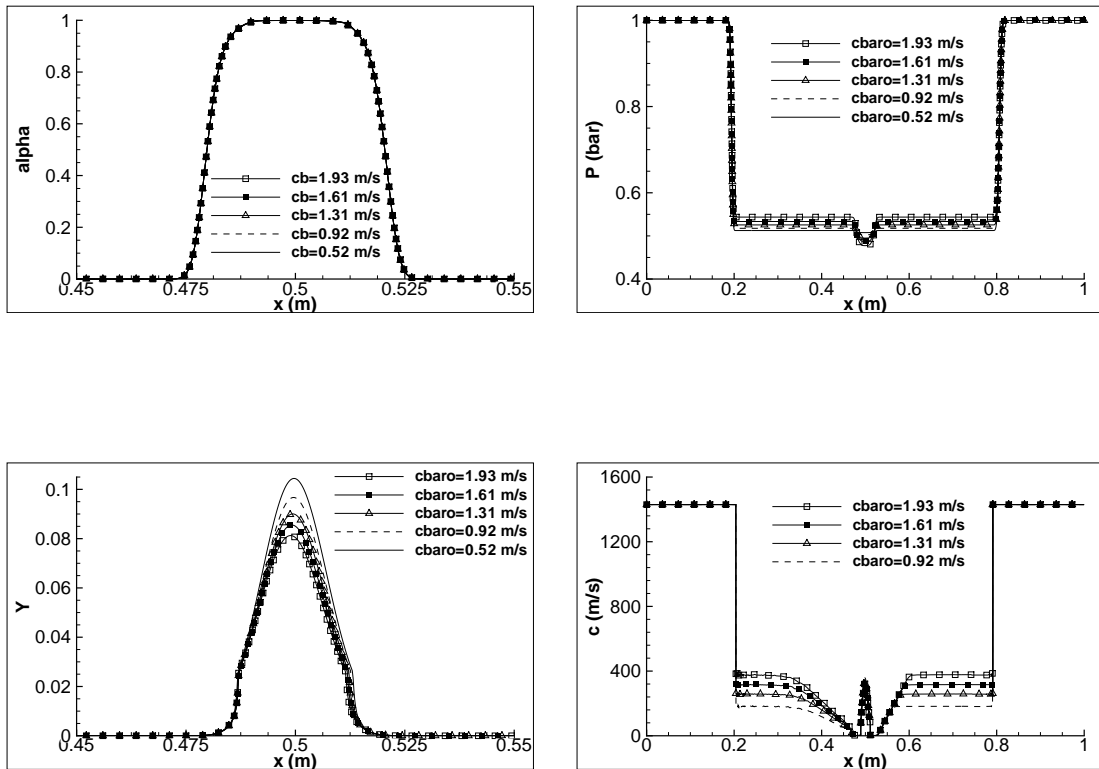
Figure 3: Water-gas double rarefaction with cavitation $|u| = 2$ m/s, influence of c_{baro}, 4-equation barotropic model, Rusanov scheme, mesh 5000 cells, $t = 3.2$ms. Void ratio, mixture speed of sound and pressure.
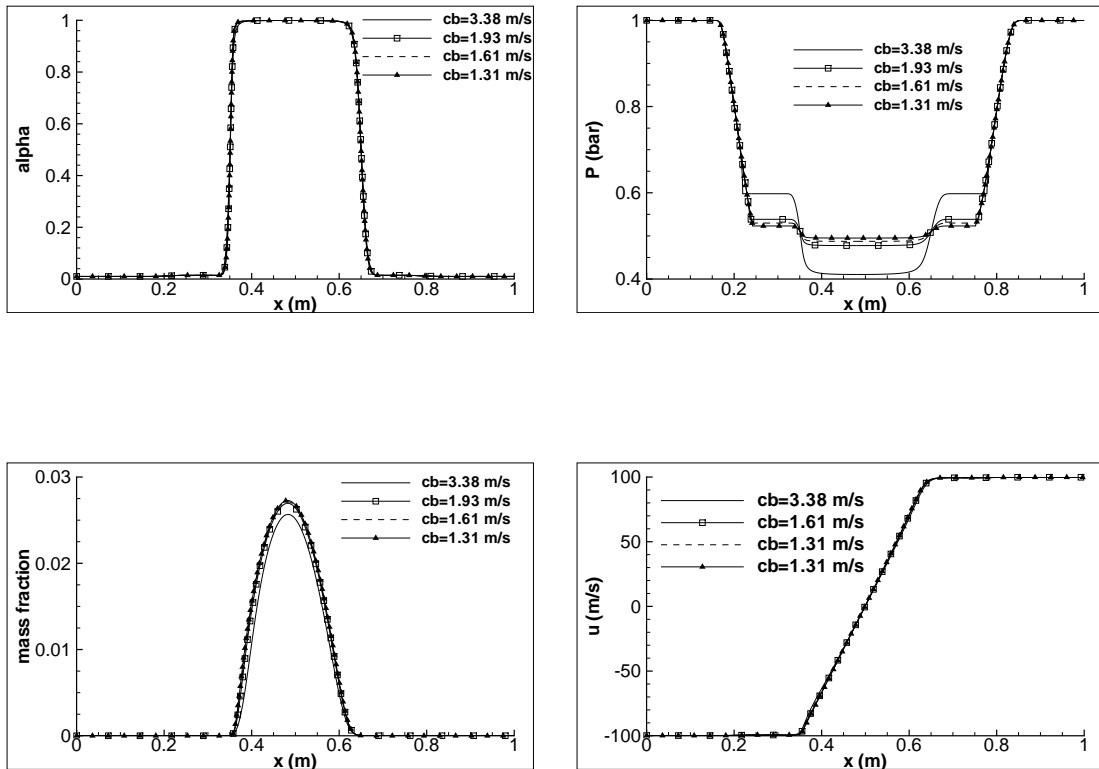
Figure 4: Water-gas double rarefaction with cavitation $|u| = 100$ m/s, influence of c_{baro}, 4-equation barotropic model, Rusanov scheme, mesh 5000 cells, $t = 1.5$ ms. Void ratio, mass fraction, pressure and velocity.
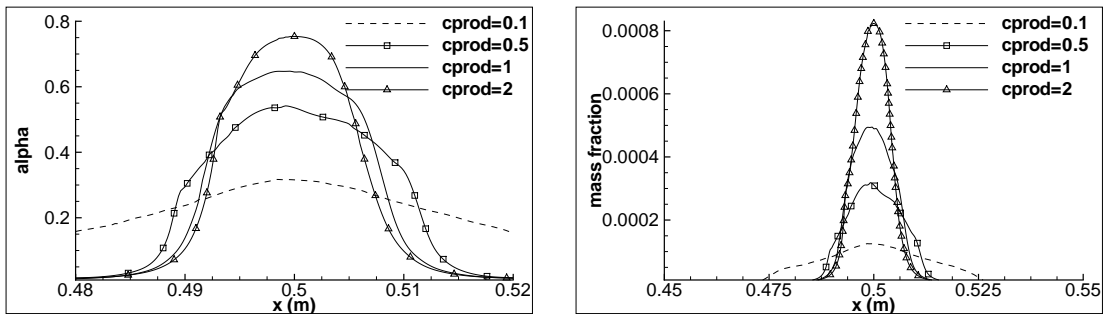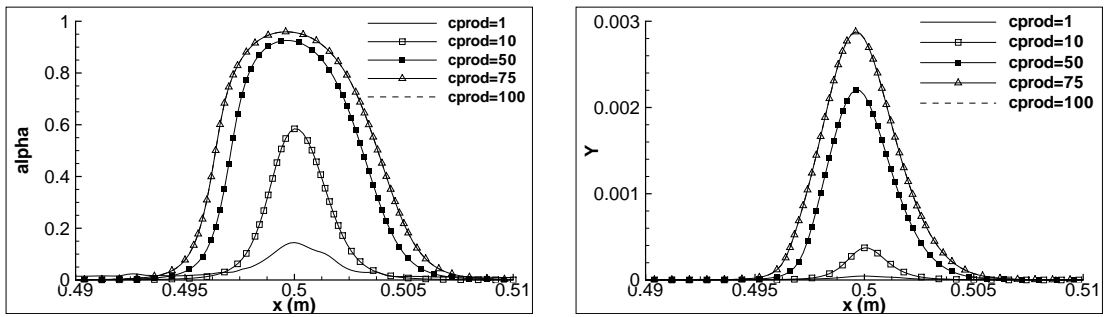
Figure 5: Water-gas double rarefaction with cavitation $|u| = 2$ m/s, influence of C_{prod}, 4-equation empirical model, Rusanov scheme, mesh 5000 cells, $t = 3.2$ms. Void ratio and mass fraction.
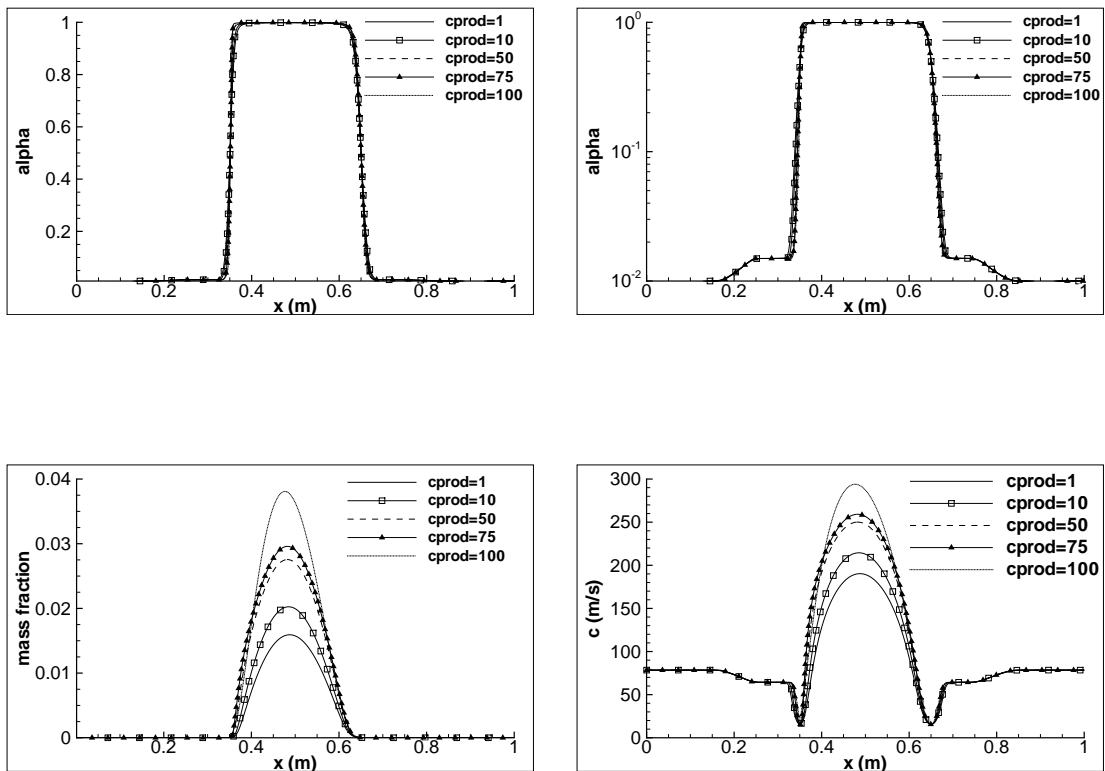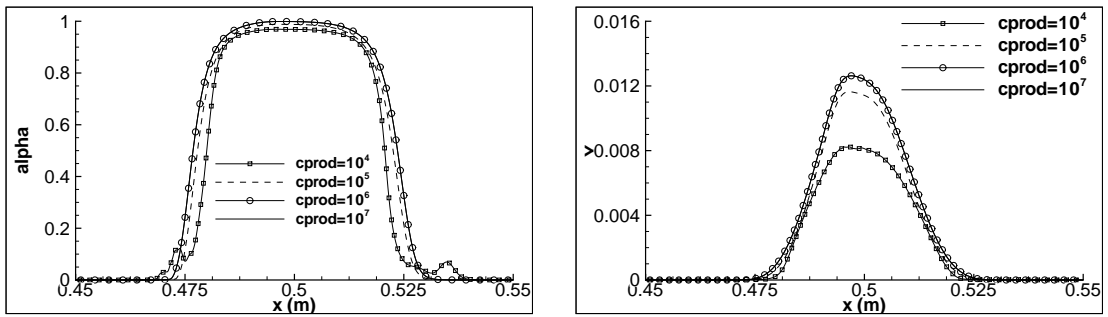
Figure 6: Water-gas double rarefaction with cavitation $|u| = 100$ m/s, influence of C_{prod}, 4-equation empirical model, Rusanov scheme, mesh 5000 cells, $t = 1.5$ ms. Void ratio, mass fraction and mixture speed of sound.
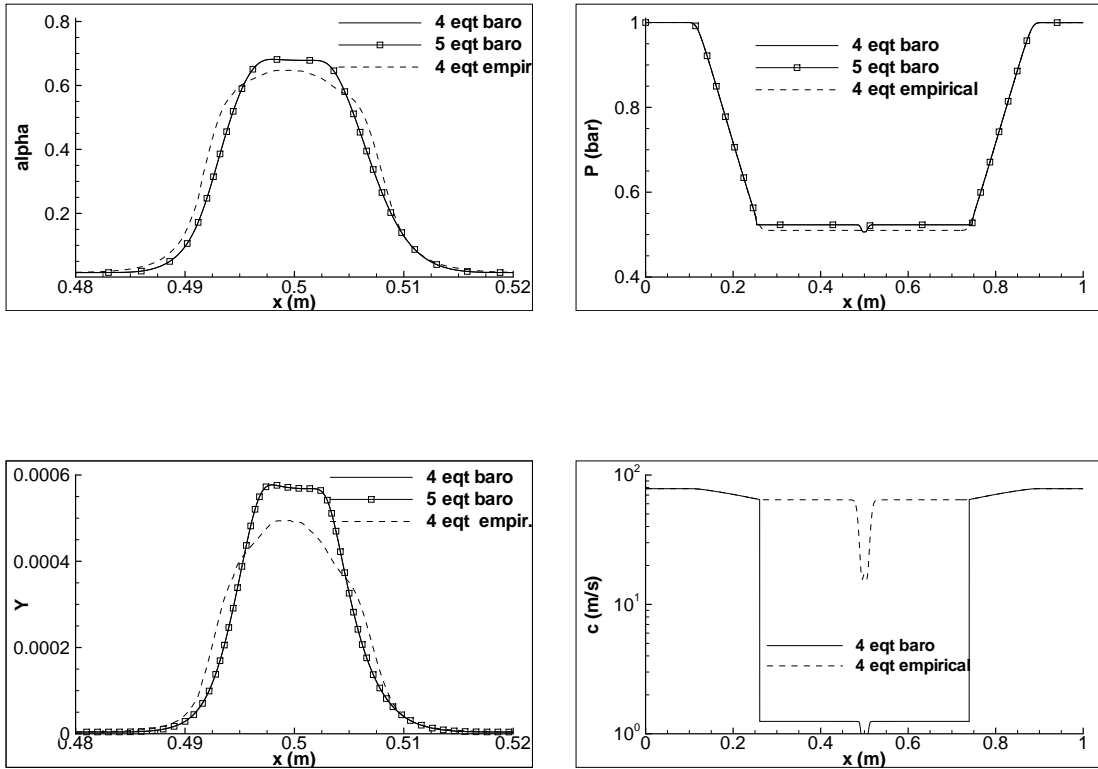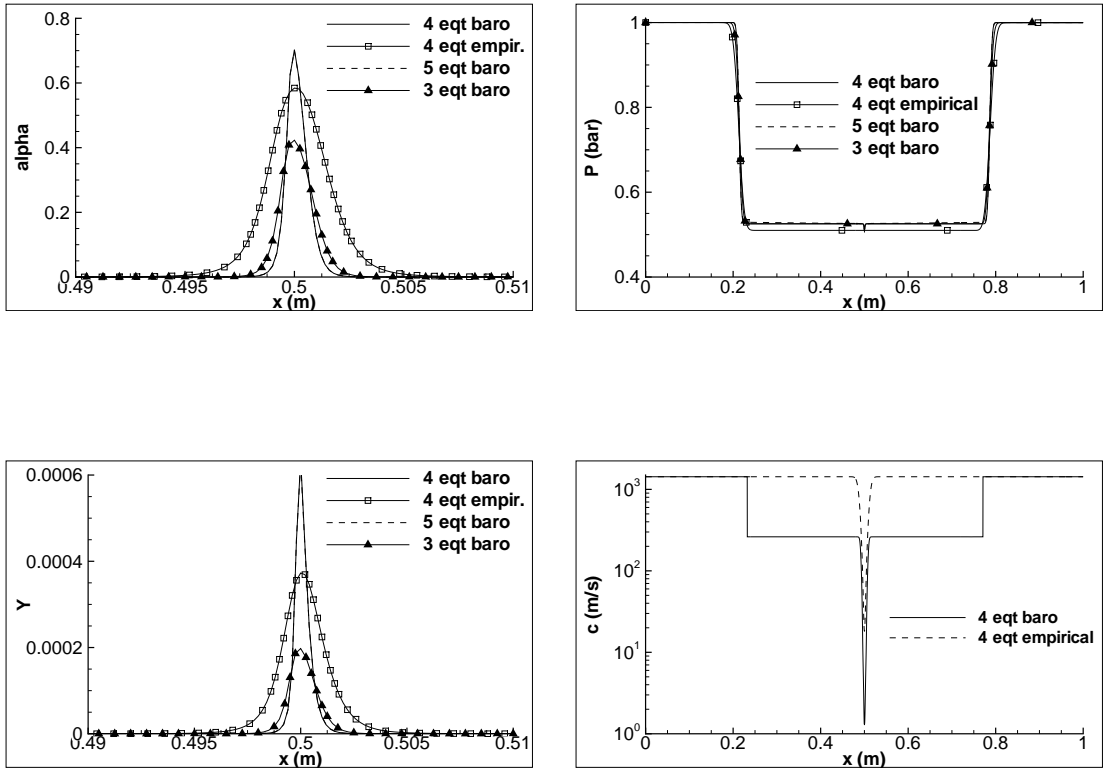
Figure 7: Water-gas double rarefaction with cavitation $|u| = 2$ m/s, models comparison, Rusanov scheme, mesh 5000 cells, $t = 3.2$ms. Void ratio, mass fraction, pressure and mixture speed of sound.
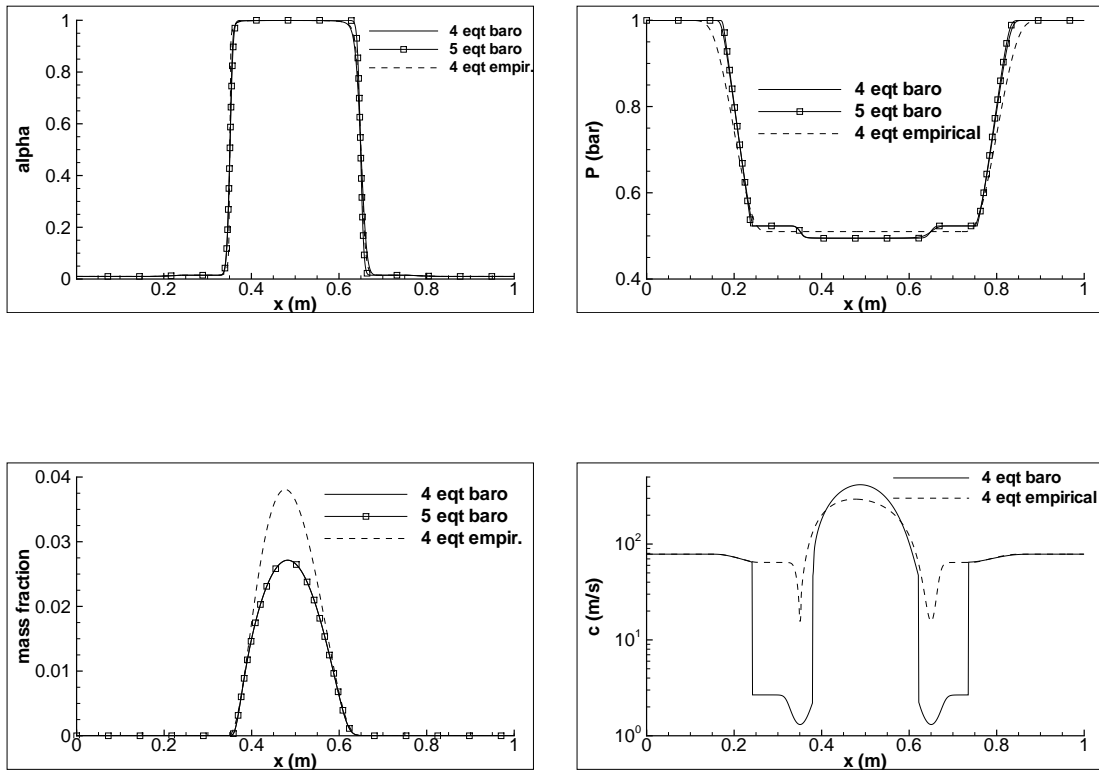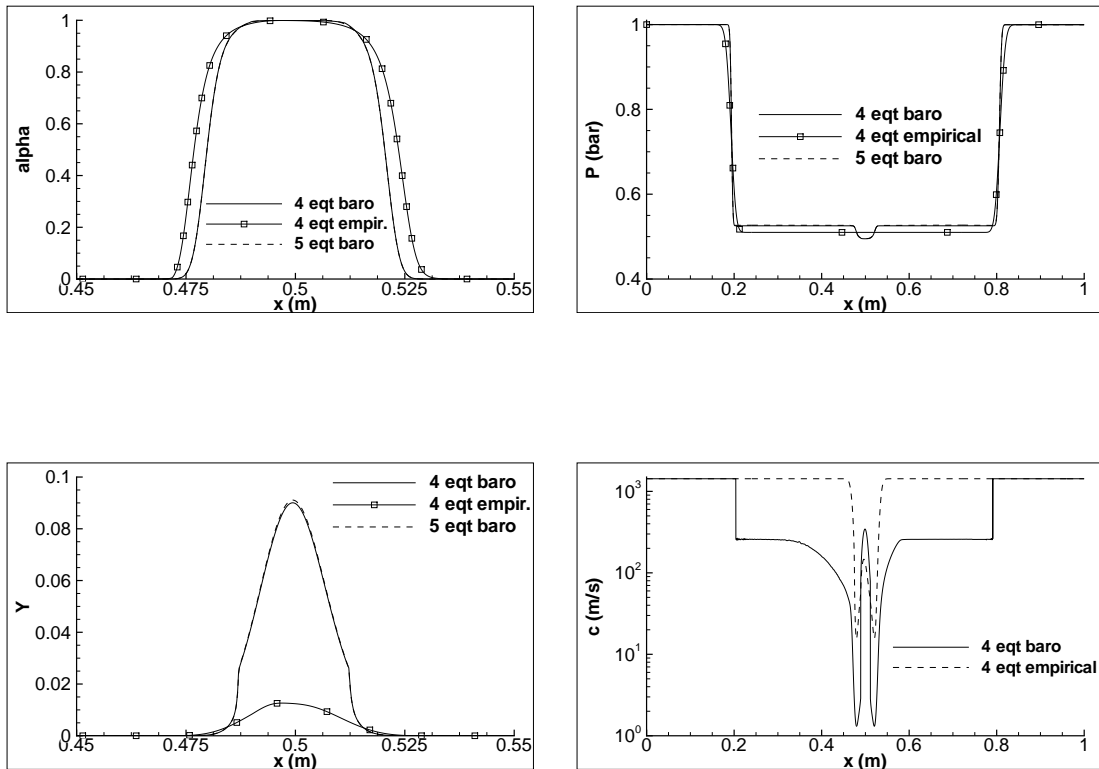
Figure 8: Water-gas double rarefaction with cavitation $|u| = 100$ m/s, models comparison, Rusanov scheme, mesh 5000 cells, $t = 1.5$ ms. Void ratio, mass fraction, pressure and mixture speed of sound.

Figure 9: Water double rarefaction with cavitation $|u| = 100$ m/s, influence of c_{baro}, 4-equation barotropic model, Rusanov scheme, mesh 5000 cells, $t = 0.2$ ms. Void ratio, mass fraction, pressure and mixture speed of sound.

Figure 10: Water double rarefaction with cavitation $|u| = 2$ m/s, influence of C_{prod}, 4-equation empirical model, Rusanov scheme, mesh 5000 cells, $t = 0.2$ ms. Void ratio and mass fraction.

Figure 11: Water double rarefaction with cavitation $|u| = 100$ m/s, influence of c_{prod}, 4-equation empirical model, Rusanov scheme, mesh 5000 cells, $t = 0.2$ ms. Void ratio and mass fraction.

Figure 12: Water double rarefaction with cavitation $|u| = 2$ m/s, models comparison, Rusanov scheme, mesh 5000 cells, $t = 0.2$ ms. Void ratio, mass fraction, pressure and mixture speed of sound.
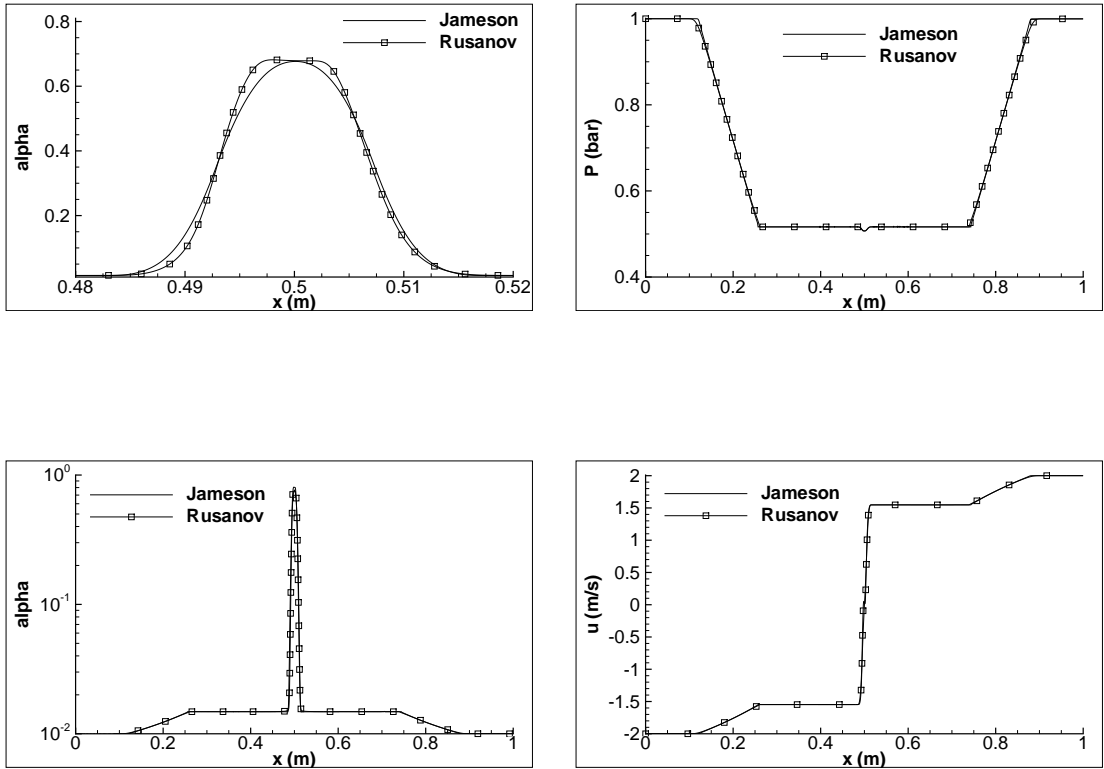
Figure 13: Water-gas double rarefaction with cavitation $|u| = 100$ m/s, models comparison, Rusanov scheme, mesh 5000 cells, $t = 0.2$ ms. Void ratio, mass fraction, pressure and mixture speed of sound.

Figure 14: Water-gas double rarefaction with cavitation $|u| = 2$ m/s, numerical schemes comparison, 4-equation barotropic model, $c_{baro} = 1.31$ m/s, mesh 5000 cells, $t = 3.2$ms. Void ratio, pressure and velocity.
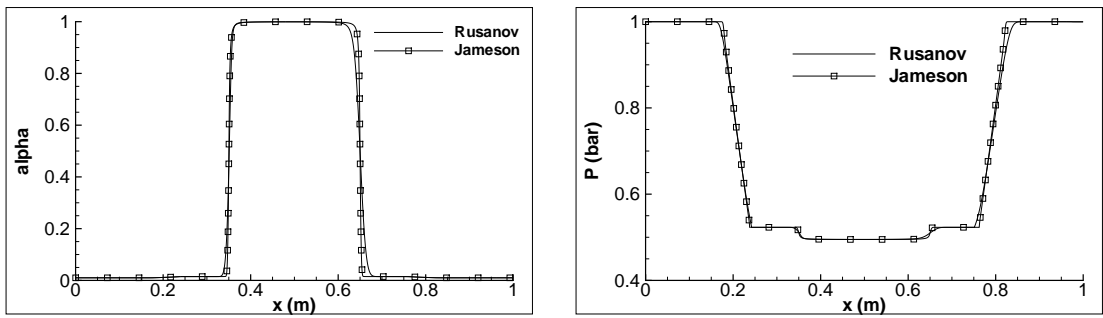
Figure 15: Water-gas double rarefaction with cavitation $|u| = 100$ m/s, numerical schemes comparison, 4-equation barotropic model, $c_{baro} = 1.31$ m/s, mesh 5000 cells, $t = 1.5$ ms. Void ratio and pressure.
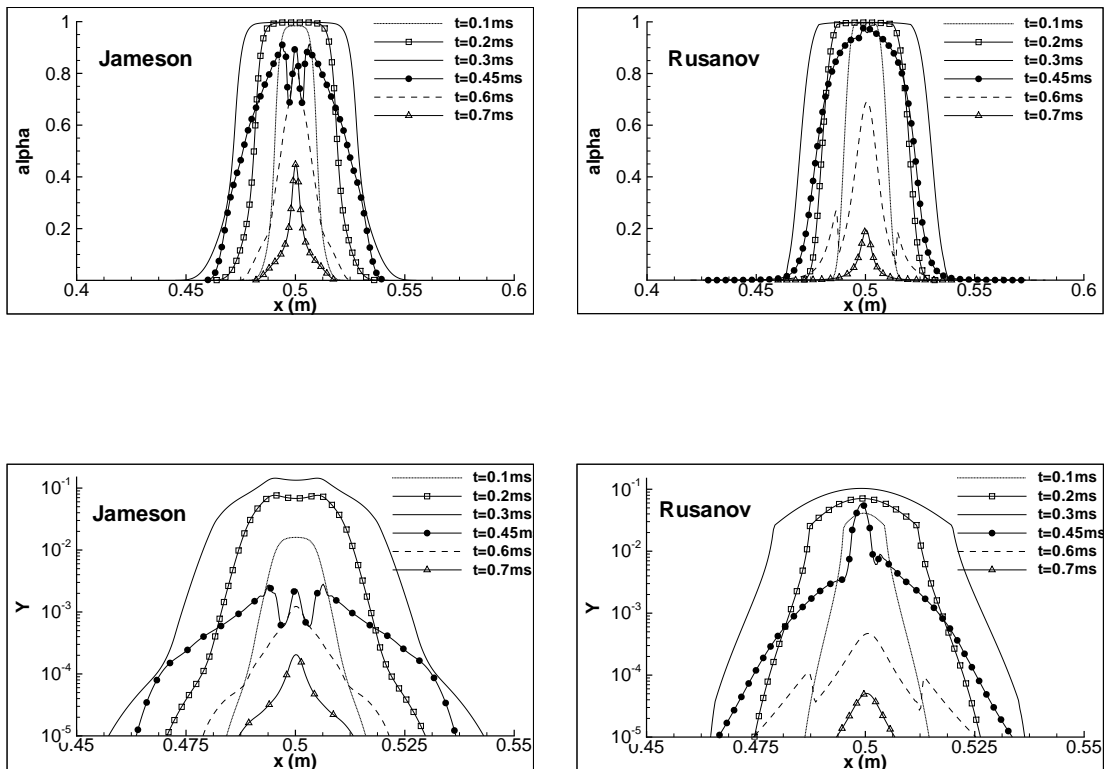
64

Figure 16: Shock-cavitation interaction, Jameson versus Rusanov scheme, 4-equation barotropic model, $c_{baro} = 1.31$ m/s, mesh 5000 cells. Void ratio and mass fraction at different times.
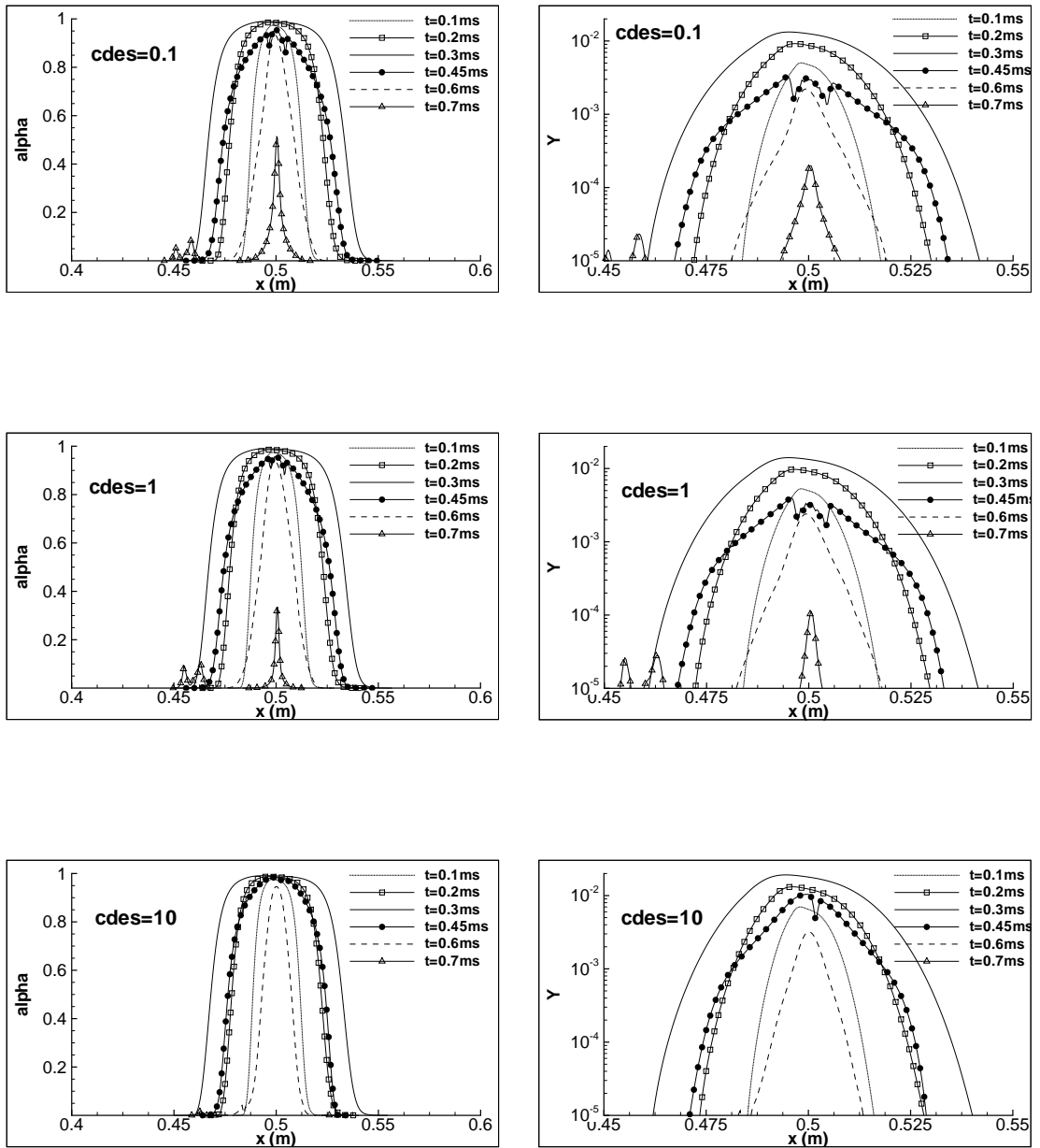
Figure 17: Shock-cavitation interaction, 4-equation empirical model with $c_{prod} = 10^6$, influence of c_{des}, Rusanov scheme, mesh 5000 cells. Void ratio and mass fraction at different times.
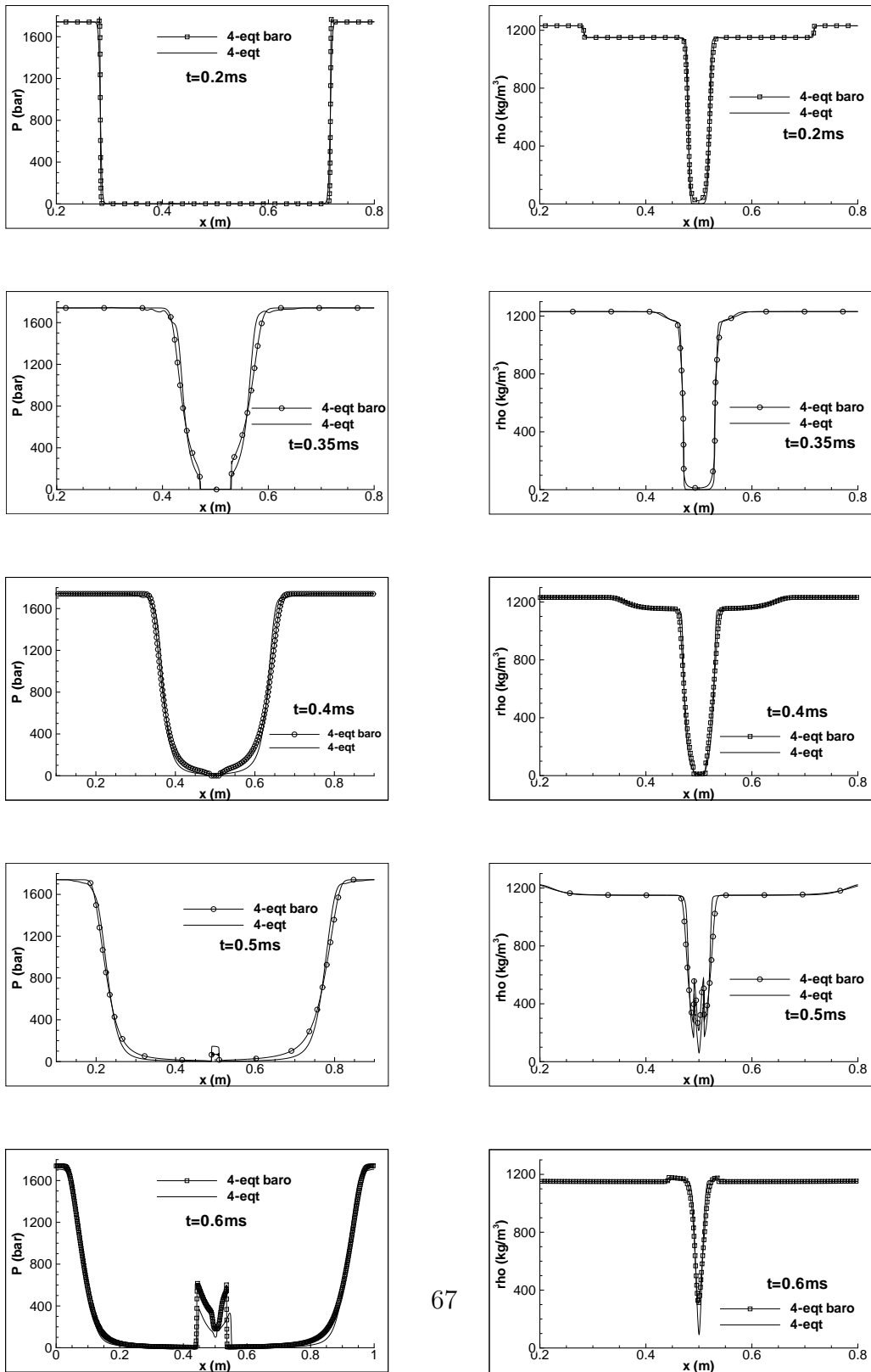
66

Figure 18: Shock-cavitation interaction, models comparison, Rusanov scheme, mesh 5000 cells. Pressure and density at different times.